

Polarized Radiation Transfer in Neutron Star Surface Layers

Joseph A. Barchas,^{1,2*} Kun Hu² and Matthew G. Baring²

¹*Natural Sciences, Southwest Campus, Houston Community College, 5601 W. Loop S., Houston, Texas 77081, USA*

²*Department of Physics and Astronomy - MS 108, Rice University, 6100 Main Street, Houston, Texas 77251-1892, USA*

Accepted November 9, 2020; Received October 19, 2020; in original form August 31, 2020.

ABSTRACT

The study of polarized radiation transfer in the highly-magnetized surface locales of neutron stars is of great interest to the understanding of accreting X-ray pulsars, rotation-powered pulsars and magnetars. This paper explores scattering transport in the classical magnetic Thomson domain that is of broad applicability to these neutron star classes. The development of a Monte Carlo simulation for the polarized radiative transfer is detailed: it employs an electric field vector formalism to enable a breadth of utility in relating linear, circular and elliptical polarizations. The simulation can be applied to any neutron star surface locale, and is adaptable to accretion column and magnetospheric problems. Validation of the code for both intensity and Stokes parameter determination is illustrated in a variety of ways. Representative results for emergent polarization signals from surface layers are presented for both polar and equatorial magnetic locales, exhibiting contrasting signatures between the two regions. There is also a strong dependence of these characteristics on the ratio of the frequency ω of a photon to the cyclotron frequency $\omega_B = eB/mc$. Polarization signatures for high opacity domains are presented, highlighting compact analytic approximations for the Stokes parameters and anisotropy relative to the local field direction for an extended range of frequencies. These are very useful in defining injection conditions deep in the simulation slab geometries, expediting the generation of emission signals from highly opaque stellar atmospheres. The results are interpreted throughout using the polarization characteristics of the magnetic Thomson differential cross section.

Key words: magnetic fields – radiative transfer – stars: magnetars – stars: neutron – X-rays: stars

1 INTRODUCTION

Observations of thermal emission from both isolated and accreting neutron stars have provided a richness of information about their surfaces and interiors. Radii of isolated neutron stars can be estimated or constrained by applying the Stefan-Boltzmann law to their quasi-thermal spectra (Potekhin 2014). Soft X-ray pulse profiles of younger and middle-aged neutron stars have been used to estimate geometric parameters like the sizes and locales of hot spots and observer viewing angles to the spin axes: see Gotthelf et al. (2010) for an example of central compact object, and Younes et al. (2020) for a magnetar. For much older neutron stars, recycled pulsars (PSRs), pulse profiles of atmospheric X rays from millisecond PSR J0030+0451 by the Neutron Star Interior Composition Explorer (*NICER*) have enabled precise

mass and radius measurements (Riley et al. 2019; Miller et al. 2019). Spectral features such as absorption lines help to estimate the gravitational redshifts (Hambaryan et al. 2011) and thereby also inform mass-to-radius ratios. Comparisons between surface temperatures from cooling neutron stars and theoretical cooling curves yield insights into the thermal heating and neutrino transport in neutron star interiors, deriving constraints on the equation of state (Yakovlev & Pethick 2004). All these probes can leverage a sophisticated understanding of neutron star atmospheres, which serves as the principal objective of this paper.

Of great interest is the persistent soft X-ray emission of magnetars, neutron stars that possess super-strong magnetic fields. Magnetars’ surface fields ($B_p \sim 10^{13} - 10^{15}$ G) and relative young ages are inferred directly from their long spin periods ($P \sim 2 - 12$ s) and large spin-down rates ($\dot{P} \sim 10^{-14} - 10^{-10}$ s s^{-1}), presuming that their rotational spin down is due to magnetic dipole torques (e.g., see Kouveliotou et al. 1998). Magnetars have historically been divided into two observational groups: Soft-Gamma Repeaters

* E-mail: joseph.barchas@hccs.edu (JAB); kh38@rice.edu (KH); baring@rice.edu (MGB)

(SGRs) and Anomalous X-ray Pulsars (AXPs). However, the observed quiescent emission from SGRs and the discovery of SGR-like bursts in several AXPs diluted the difference between the two groups, suggesting a “unification paradigm” where SGRs and AXPs belong to a single class. On the theoretical side, Duncan & Thompson (1992) and Thompson & Duncan (1996) postulated the fireball scenario where the flare emission is triggered by sub-surface magnetic activity. This focuses on magnetic stresses in the crust and structural rearrangements and partial decay of the sub-surface fields (Thompson & Duncan 1995, 2001).

The persistent soft X-ray signals from magnetars are very bright, with typical luminosities of $L_X \sim 10^{35} \text{erg s}^{-1}$, often exceeding their rotational energy loss rates. The spectra of this emission can be approximately fit using blackbodies of temperature $\sim 0.3 - 0.6 \text{keV}$, connected to a soft power-law tail with photon index $\lesssim 2 - 4$ (e.g., Mereghetti 2008; Viganò et al. 2013). These temperatures are higher than those of typical isolated neutron stars – see Becker (2009) for a review of X-ray pulsar emission. The thermal component likely comes from the stellar surface, providing information about the physical properties of its atmosphere, like chemical composition, ionization equilibrium, and the state of matter. Pulse profiles of magnetars constrain the locale of the emission region, and thereby help improve the understanding of sub-surface thermal heat transport, and informing paradigms of particle bombardment of the surface (Beloborodov & Li 2016). For some magnetars, the best fit is obtained using a two-blackbody model, which is possibly a signature of temperature gradients across the stellar surface (Gottlieb & Halpern 2005).

Models for magnetic neutron star surface emissions have been constructed by Shibano et al. (1992), Pavlov et al. (1994), Zavlin, Pavlov & Shibano (1996) and Zane et al. (2000), considering fully-ionized hydrogen or helium atmospheres with moderate magnetic fields $\sim 10^{13} \text{G}$. Partially-ionized atmosphere models have been explored by Ho et al. (2003), Potekhin et al. (2004), Ho et al. (2008) and Suleimanov et al. (2009), using sophisticated opacity information and updated equations of state. Atmosphere models addressing the magnetar field domain were treated by Ho & Lai (2001), Özel (2001), Ho & Lai (2003), Özel (2003), Adelsberg & Lai (2006) and Taverna et al. (2020). Since the fields of magnetars generally exceeds the critical field $B_{\text{cr}} = 4.414 \times 10^{13} \text{Gauss}$, detailed consideration of the polarization of the magnetized quantum vacuum is necessary (Lai & Ho 2003). In addition, thermal emission from condensed surfaces at relatively low temperatures was studied by Turolla et al. (2004) and Medin & Lai (2007). For magnetic fields $\lesssim 10^{12} \text{G}$, this magnetic condensation is expected to be minimal, and the atmospheres are likely fully ionized (Medin & Lai 2006, 2007).

A common feature of these previous studies is that they use scattering and free-free opacity to mediate the photon transport in terms of two orthogonal polarization modes. These opacities help to support the atmosphere hydrostatically and shape the calculated spectra, which deviate substantially from a pure Planck form. Furthermore, X-ray emission from the surfaces of magnetars is expected to be polarized, because the strong magnetic fields introduce anisotropy to the plasma medium, the quantum vacuum, and the scattering process, as is highlighted here. These in-

teresting physics elements can be probed using polarimetric measurements of magnetars in the soft X-ray band, which are expected to be provided by future missions like IXPE¹ (Weisskopf et al. 2016) and eXTP (Zhang et al. 2016). Such polarimetry introduces an extra dimension to diagnostics of source physical properties that complement spectroscopy, and should permit the detection of the QED vacuum effect from magnetar atmospheres (see Taverna et al. 2020).

In this paper, we detail the construction of a new Monte Carlo simulation of the magnetic Thomson scattering of polarized X-rays in neutron star surface layers. In contrast to previous studies, we simulate the transport via a tracking of wave electric field vectors. This encapsulates full polarization information, linear and circular and their interplay throughout. The code does not presently treat self-consistent hydrostatic atmospheric structure and the free-free opacity that dominates (Ho & Lai 2001) at photon energies below around 1–2 keV and deep in the atmosphere. Thus, the simulation is readily applied to outer atmospheres and is adaptable to the more tenuous environments of magnetar magnetospheres. The simulation is developed in the special case of zero dispersion in order to enable its validation and a detailed understanding of emergent polarization signatures; it is routinely extendable to treat elliptical eigenmodes of propagation in dispersive media. Our Monte Carlo code generates angular distributions of intensity and Stokes parameters for arbitrary field orientations and a representative range of photon frequencies. The code is validated by direct comparison of results with those from prior investigations.

Although our present focus is on surface layers of magnetars and neutron stars of lesser magnetizations, the Monte Carlo technique can be easily extended to treat Comptonization in hot plasmas, which is important in the context of other phenomena like accreting X-ray pulsars and magnetar bursts and giant flares. The atmosphere results presented here can serve as a general guide to the expectations for photospheric outer envelopes of optically-thick magnetospheric bursts in magnetars (Taverna & Turolla 2017). Detailed simulations of the radiation transport in the photospheres of both magnetar fireballs and accretion column of X-ray pulsars are of interest of future hard X-ray polarimeters, and will be the subject of future extensions of the code.

The paper begins with a review of elements of the classical electrodynamical formulation of magnetic Thomson scattering and the description of polarization in Sec. 2. In Sec. 3 we describe the Monte Carlo technique underpinning the *MAGTHOMSCATT* code, including sampling and binning. Intensity and polarization results for slab surface volumes in are detailed in Sec. 4 for two special locales on a neutron star surface, the magnetic pole and the equator. Comparisons with previous works are forged therein as a means of code validation. Polarization results at high opacity are given in Sec. 5, together with empirical functions for anisotropic photon distribution and Stokes parameters. The resultant understanding of this polarization information in such high opacity domains facilitates the accurate modeling of complete atmospheres with simulations possessing modest computational demands. Some contextual discussions for neutron star applications are offered in Sec. 6.

¹ <https://ixpe.msfc.nasa.gov/>

2 POLARIZED RADIATION TRANSFER IN STRONG MAGNETIC FIELDS

The technical approach adopted in the simulation we detail in this paper models photon transport and magnetic scattering using an electric field vector formalism. This distinguishes it from previous studies that have tracked Stokes parameter information (Whitney 1991a,b) or linearly polarized states in the resonant cyclotron approximation (Fernández & Thompson 2007; Nobili et al. 2008; Fernández & Davis 2011). This electric vector approach is more fundamental, more general, and is elegant in how it isolates key characteristics of the scattering transport, identifying the critical interplay between linear and circular polarizations that is missing in most works. Employment of the tracking of electric (polarization) vectors also affords greater versatility for future extensions, like adding up emission from extended regions on the stellar surface or perhaps from magnetospheric locales, general relativistic polarization transport and dispersive propagation out to an observer at infinity. Such versatility is not permitted by pure Stokes parameter transport approaches such as in Whitney (1991a,b).

The structure of the radiative transfer simulation described in Sec. 3 is to inject polarized light waves at the base of an upper atmosphere where free-free opacity is low, propagate them as discrete photons, scattering them as classical electromagnetic waves in the magnetic Thomson domain, and eventually allow them to escape at the top of the atmospheric slab. The simulation will assume an effectively cold plasma, which well approximates the outer surface layers of a neutron star. Given the focus on the simulation development and validation, dispersive influences due to warm plasma and the quantum magnetic vacuum will be neglected, their treatment being deferred to future stages of our program.

The intensity and polarization of a classical, transverse electromagnetic wave can be described with a *complex* electric field 3-vector \mathbf{E} that is orthogonal to the direction of propagation \mathbf{k} :

$$\mathbf{E} = \mathbf{E}_0 \exp\{i[\mathbf{k} \cdot \mathbf{r} - \omega t - \phi(t)]\} = \mathcal{E}(\mathbf{r}, t) e^{-i\omega t}. \quad (1)$$

The magnetic field component $\mathbf{B} = \hat{\mathbf{k}} \times \mathbf{E}$ of this wave is then automatically captured and trivially determined. The polarization vector $\mathcal{E}(\mathbf{r}, t)$ incorporates the spatial dependence, which usually factors out of measures when time averages of the field are taken; we will ignore it hereafter.

2.1 Magnetic Thomson Scattering

The classical electromagnetic theory of electron scattering in the absence of external fields is detailed in texts such as Jackson (1975); Landau & Lifshitz (1975); Rybicki & Lightman (1979). Such Thomson scattering formalism is routinely adapted to treat the case of gyration motion of electrons in a magnetic field, and a seminal formulation was presented in Canuto et al. (1971) in the context of plasma dispersion. The classical formulation is distilled here to identify elements germane to the simulation algorithms of Sec. 3, and the presentation of results in Secs. 4 and 5.

The incident electromagnetic wave has a direction of propagation given by the unit vector $\hat{\mathbf{k}}_i$, and an electric field $\mathbf{E}(t) = \mathcal{E}_i e^{-i\omega t}$, with $\mathcal{E}_i \cdot \hat{\mathbf{k}}_i = 0$. The oscillating wave field drives the acceleration of an electron subject to the

influence of a magnetic field $\mathbf{B} \equiv B\hat{\mathbf{B}}$, motion described by the Newton-Lorentz equation:

$$m_e \frac{d\mathbf{v}(t)}{dt} = -e\mathbf{E}(t) - \frac{e}{c} \mathbf{v}(t) \times \mathbf{B}. \quad (2)$$

Since $\mathbf{E}(t) \propto e^{-i\omega t}$, it is readily seen that the time dependence of the acceleration contains the same exponential factor: $\mathbf{a} \equiv d\mathbf{v}/dt \propto e^{-i\omega t}$ with velocity $\mathbf{v} = \mathbf{a}/(-i\omega) \propto e^{-i\omega t}$ also. By factoring out the time dependence, the induced acceleration then satisfies

$$\mathbf{a} e^{i\omega t} = -\frac{e}{m_e} \frac{\boldsymbol{\alpha} |\mathcal{E}_i|}{\omega^2 - \omega_B^2}, \quad (3)$$

where

$$\boldsymbol{\alpha} = \omega^2 \hat{\boldsymbol{\mathcal{E}}}_i - i\omega\omega_B \hat{\boldsymbol{\mathcal{E}}}_i \times \hat{\mathbf{B}} - \omega_B^2 (\hat{\boldsymbol{\mathcal{E}}}_i \cdot \hat{\mathbf{B}}) \hat{\mathbf{B}}, \quad (4)$$

and $\omega_B = eB/m_e c$ is the electron cyclotron frequency. In general, $\hat{\mathbf{k}}_i \times \hat{\mathbf{B}} \neq \mathbf{0}$ so that $\mathcal{E}_i \cdot \hat{\mathbf{B}} \neq \mathbf{0}$. We have introduced the scaled incident polarization vector $\hat{\boldsymbol{\mathcal{E}}}_i = \mathcal{E}_i/|\mathcal{E}_i|$ to simplify ensuing expressions for the differential and total cross section. The motion is clearly oscillatory at the driving frequency ω , generally with different amplitudes in each of the three dimensions, leading to elliptical polarization for the scattered photon. The $\hat{\boldsymbol{\mathcal{E}}}_i \times \hat{\mathbf{B}}$ term is the driver for circular polarization, and its influence is maximized near the cyclotron frequency.

The accelerating, non-relativistic charge radiates a scattered wave. The dipole radiation formula can be employed for an accelerating electron to obtain the electric field after scattering (Landau & Lifshitz 1975):

$$\mathbf{E}_f(\mathbf{r}, t) \equiv \frac{r_0}{R} \mathcal{E}_f e^{-i\omega t} = -\frac{e}{Rc^2} \hat{\mathbf{k}}_f \times (\hat{\mathbf{k}}_f \times \boldsymbol{\alpha}) \quad (5)$$

where $\hat{\mathbf{k}}_f$ is the direction of propagation of the scattered wave. The frequency of the outgoing wave is just that of the incoming one, the signature of Thomson scattering. Here, R is the distance from the oscillating/radiating dipole to a point of observation, and $r_0 = e^2/m_e c^2$ is the classical electron radius. Inserting the acceleration from Eq. (3),

$$\hat{\boldsymbol{\mathcal{E}}}_f \equiv \frac{\mathcal{E}_f}{|\mathcal{E}_f|} = \frac{\hat{\mathbf{k}}_f \times (\hat{\mathbf{k}}_f \times \boldsymbol{\alpha})}{\omega^2 - \omega_B^2}. \quad (6)$$

Thus the transversality condition $\mathcal{E}_f \cdot \hat{\mathbf{k}}_f = 0$ follows. The dipole radiation formalism then delivers the differential cross section for magnetic Thomson scattering via the ratio $R^2 |\mathcal{E}_f|^2 / |\mathcal{E}_i|^2$ of final to initial wave Poynting fluxes:

$$\frac{d\sigma}{d\Omega_f} = r_0^2 \hat{\boldsymbol{\mathcal{E}}}_f \cdot \hat{\boldsymbol{\mathcal{E}}}_f^* = r_0^2 \frac{(\hat{\mathbf{k}}_f \times \boldsymbol{\alpha}) \cdot (\hat{\mathbf{k}}_f \times \boldsymbol{\alpha}^*)}{(\omega^2 - \omega_B^2)^2}. \quad (7)$$

This distillation has employed Eqs. (4) and (6). Using a polarization tensor, Eq. (7) can be modified to treat dispersive cases, for example in accounting for the dielectric response of a plasma (Canuto et al. 1971; Ventura 1979).

Employing a standard vector identity for the numerator of Eq. (7), it is routinely integrated over solid angles $d\Omega_f$ to yield the total scattering cross section:

$$\sigma = \frac{8\pi}{3} r_0^2 \frac{\boldsymbol{\alpha} \cdot \boldsymbol{\alpha}^*}{(\omega^2 - \omega_B^2)^2}. \quad (8)$$

Details of the derivation are posited in Appendix A. Further,

expanding $\boldsymbol{\alpha} \cdot \boldsymbol{\alpha}^*$ using Eq. (4) then quickly gives

$$\sigma = \frac{\sigma_{\text{T}}}{(\omega^2 - \omega_{\text{B}}^2)^2} \left[\omega^4 + \omega_{\text{B}}^2(\omega_{\text{B}}^2 - 2\omega^2) \left| \hat{\boldsymbol{\mathcal{E}}}_i \cdot \hat{\boldsymbol{B}} \right|^2 + \omega^2 \omega_{\text{B}}^2 \left| \hat{\boldsymbol{\mathcal{E}}}_i \times \hat{\boldsymbol{B}} \right|^2 + 2i\omega^3 \omega_{\text{B}} \hat{\boldsymbol{B}} \cdot (\hat{\boldsymbol{\mathcal{E}}}_i \times \hat{\boldsymbol{\mathcal{E}}}_i^*) \right], \quad (9)$$

where $\sigma_{\text{T}} = 8\pi r_0^2/3$ is the familiar Thomson cross section in the absence of an external field. The term proportional to $i\omega^3\omega_{\text{B}}$ is actually real: this character can be established by adding $\hat{\boldsymbol{\mathcal{E}}}_i \times \hat{\boldsymbol{\mathcal{E}}}_i^*$ to its complex conjugate to demonstrate that this vector is always purely imaginary. Observe that because of transversality, $\hat{\boldsymbol{\mathcal{E}}}_i \times \hat{\boldsymbol{\mathcal{E}}}_i^*$ is parallel to $\hat{\boldsymbol{k}}_i$, a result that is quickly established using the expansion of the vector triple product $\hat{\boldsymbol{k}}_i \times (\hat{\boldsymbol{\mathcal{E}}}_i \times \hat{\boldsymbol{\mathcal{E}}}_i^*) \equiv \mathbf{0}$. Eq. (9) can be evaluated for any polarization configuration for the incident photon, as is done in Appendix B. These vector forms for the differential and the total cross sections appear not to have been derived before, and complement other expositions in the literature (e.g., Hamada, & Kanno 1974; Börner, & Meszaros 1979).

Total cross sections for the linearly-polarized states \perp and \parallel are presented in Fig. 10 in Appendix B, illustrating the prominence of the resonance at the cyclotron frequency, $\omega = \omega_{\text{B}}$. In the classical picture, radiation reaction consumes some of the kinetic energy of the driven electron, leading to an extra term in the dynamical equation in Eq. (2) (e.g., Landau & Lifshitz 1975). This yields damped waves with solutions approximated by $\omega \rightarrow \omega + i\Gamma/2$ for cyclotron radiative width Γ , so that a Lorentz profile proportional to $1/[(\omega - \omega_{\text{B}})^2 + \Gamma^2/4]$ replaces the divergent factor $1/(\omega - \omega_{\text{B}})^2$. The same type of Breit-Wigner modification arises in a quantum description (e.g. Harding & Daugherty 1991), where the width is now due to the finite cyclotron decay lifetime of the intermediate virtual electron state. Accordingly, the divergence is truncated, yielding finite values for the cross section that are of the order of $(\omega_{\text{B}}/\Gamma)^2\sigma_{\text{T}}$ when the magnetic field is highly-subcritical, $B \ll B_{\text{cr}}$; details can be found in the papers by Baring, Wadiasingh & Gonthier (2011) and Gonthier et al. (2014).

2.2 Parameterizing Polarization

The electric field vector approach to handling transport and scattering of individual photons is elegant and powerful. Yet, for the purposes of polarization accounting for large numbers of photons emergent from the simulation geometry, and for comparison with other studies, it is expedient to also adopt the convenient parameterization identified by Stokes (1851) encapsulated in the Stokes vector $\boldsymbol{S} \equiv (I, Q, U, V)$. The Stokes I parameter describes the intensity of the radiation. The Stokes Q and U parameters are related to the degree and angle of linear polarization. The Stokes parameter V captures information concerning circular polarization. In this paper, we will use the convention that the right-hand rule applies to *increasing* phases to specify the sense of $\boldsymbol{\mathcal{E}}$ rotation for a circularly polarized wave. With this convention, $V/I = 1(-1)$ corresponds to fully right- (left-) handed circularly polarized radiation.

A principal measure featuring in the simulation output and graphical illustrations of Sections 4 and 5 is the *degree of polarization* Π :

$$\Pi = \sqrt{(Q/I)^2 + (U/I)^2 + (V/I)^2}, \quad 0 \leq \Pi \leq 1. \quad (10)$$

One can similarly define the linear polarization degree $\Pi_{\text{lin}} = \Pi(V \rightarrow 0)$ by setting $V = 0$ in Eq. (10). In the Monte Carlo radiation transfer simulation that is described in Section 3, each light wave is a monochromatic photon with 100% polarization, i.e. $\Pi = 1$, regardless of whether the light is linearly, circularly or elliptically polarized. Accordingly, the construction can comfortably accommodate the elliptical eigenmodes that arise in dispersive propagation in plasma or the magnetized quantum vacuum.

The Stokes parameters for a photon can naturally be expressed in terms of its electric field vector information for general propagation directions using spherical polar coordinates rather than employing a Cartesian basis. The propagation direction $\hat{\boldsymbol{k}}$ is the radial direction, and the spherical polar angles give

$$\boldsymbol{\mathcal{E}} = \mathcal{E}_{\theta}\hat{\boldsymbol{\theta}} + \mathcal{E}_{\phi}\hat{\boldsymbol{\phi}} \equiv |\boldsymbol{\mathcal{E}}|(\hat{\boldsymbol{\mathcal{E}}}_{\theta}\hat{\boldsymbol{\theta}} + \hat{\boldsymbol{\mathcal{E}}}_{\phi}\hat{\boldsymbol{\phi}}) \quad (11)$$

for the polarization vector, with $\hat{\boldsymbol{\mathcal{E}}}_{\theta} = \mathcal{E}_{\theta}/|\boldsymbol{\mathcal{E}}|$ and $\hat{\boldsymbol{\mathcal{E}}}_{\phi} = \mathcal{E}_{\phi}/|\boldsymbol{\mathcal{E}}|$. Using the $\phi = 0$ plane for reference, with a correspond convention that $U = 0$, the Stokes parameter definition in this basis is

$$\boldsymbol{S} \equiv \begin{pmatrix} I \\ Q \\ U \\ V \end{pmatrix} = \begin{pmatrix} \langle \mathcal{E}_{\theta}\mathcal{E}_{\theta}^* \rangle + \langle \mathcal{E}_{\phi}\mathcal{E}_{\phi}^* \rangle \\ \langle \mathcal{E}_{\theta}\mathcal{E}_{\theta}^* \rangle - \langle \mathcal{E}_{\phi}\mathcal{E}_{\phi}^* \rangle \\ \langle \mathcal{E}_{\theta}\mathcal{E}_{\phi}^* \rangle + \langle \mathcal{E}_{\phi}^*\mathcal{E}_{\theta} \rangle \\ i(\langle \mathcal{E}_{\theta}\mathcal{E}_{\phi}^* \rangle - \mathcal{E}_{\phi}^*\mathcal{E}_{\theta}) \end{pmatrix}. \quad (12)$$

The brackets $\langle \dots \rangle$ signify time averages of the products of wave field components. This coordinate choice is naturally suited to a fixed observer direction, with (θ, ϕ) constituting zenith polar angles relative to the atmospheric slab, to be described in Sec. 3. One can also form a reduced Stokes parameter 3-vector $\hat{\boldsymbol{S}} = (\hat{Q}, \hat{U}, \hat{V}) \equiv (Q/I, U/I, V/I)$, using ratios of the polarization quantities of interest. These will be employed at the recording stage when waves/photons exit the atmospheric slabs.

The total cross section in Eq. (9) can be expressed using the Stokes parameters. This is best done using the normalized forms $\hat{I}_i = 1$, \hat{Q}_i and \hat{V}_i for the incident photon, noting that in our coordinate description, $\hat{U}_i = 0$ can be chosen without loss of generality. If $\theta_i = \arccos \mu_i$ is the angle of the initial photon to the magnetic field direction $\hat{\boldsymbol{B}}$, then using the polar coordinate forms for the Stokes parameters in Eq. (12), and the electric field vector form in Eq. (11), one quickly derives the result

$$\sigma = \sigma_{\text{T}} \left\{ \Sigma_{\text{B}}(\omega) \hat{I}_i + \frac{1}{2} [1 - \Sigma_{\text{B}}(\omega)] (\hat{I}_i + \hat{Q}_i) (1 - \mu_i^2) + \Delta_{\text{B}}(\omega) \hat{V}_i \mu_i \right\}, \quad (13)$$

where the frequency dependence is encapsulated in two simple functions $\Sigma_{\text{B}}(\omega)$ and $\Delta_{\text{B}}(\omega)$ defined in Appendix B in Eqs. (53) and (64), respectively. This clearly identifies the contributions of linear and circular polarizations to the scattering, to be elaborated upon in due course. Eq. (13) concurs with Eq. (4) of Whitney (1991a) and Eq. (2.26) of Barchas (2017), both of which were derived from the polarization phase matrix analysis of Chou (1986).

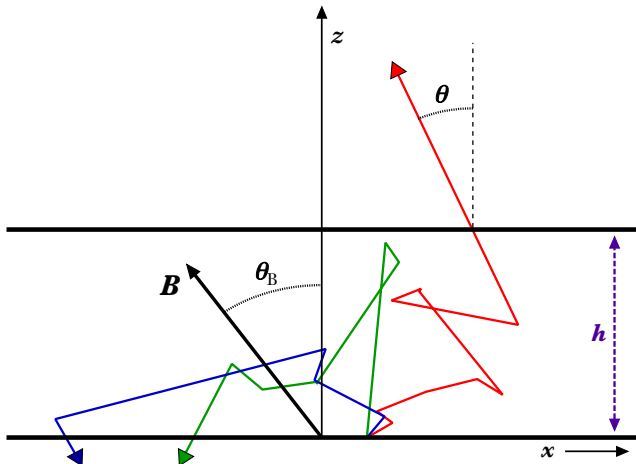


Figure 1. Simulation geometry for transfer of photons through an atmospheric slab of height h with a normal direction along the z axis (zenith) and magnetic field in the $x - z$ plane, at an angle θ_B to the local zenith. The red trajectory (projected on the $x - z$ plane) corresponds to a photon that scatters 10 times before exiting the top of the slab, reaching the observer. The blue and green trajectories are for photons that scatter and eventually exit the bottom of the slab and are therefore unobservable; they represent a sizable majority of photons (see Section 4) that are not included in the Stokes parameter data throughout.

3 MONTE CARLO SIMULATION

This Section outlines the structure of the Monte Carlo simulation that has been developed to treat scattering transfer of polarized electromagnetic waves/photons in neutron star atmospheres. This paper will focus on magnetic Thomson transport, though the technique can easily capture electron-photon energy exchange in the full Compton process. We will also restrict considerations here to locally uniform thin slabs. The familiar Thomson optical depth τ_T serves as the key parameter controlling emergent intensities, anisotropies and Stokes polarization parameters. Note that the results presented in Section 4 are applicable also to stratified atmospheric slabs with the same values of τ_T , as long as the influence of temperature gradients on $e - \gamma$ energy exchange can be neglected. A schematic diagram of the slab geometry and representative photon transfer is given in Fig. 1. The injection of photons in the simulation can be anywhere within the slab, though for our results in Section 4, it will occur at the base of the slab, i.e. at $z = 0$ in the diagram in Fig. 1 and closest to the center of the star.

The Monte Carlo technique is computationally efficient: for intensive simulations in high opacity domains, the C++ code described herein normally takes several hours or less to run on a desktop computer with a multi-core CPU. As the algorithm operates on a photon-by-photon basis, the code is parallelized. The Monte Carlo method has been applied by Whitney (1989, 1991a,b) in the context of white dwarf atmospheres, for magnetar atmospheres by Bulik & Miller (1997); Niemiec & Bulik (2006), and for magnetar coronae by Fernández & Thompson (2007); Nobili et al. (2008); Zane et al. (2011); Taverna & Turolla (2017). It serves as a complementary approach to integro-differential equation radiation transfer methods (Chandrasekhar 1960) that are common in the magnetar literature (e.g., Özel 2001; Ho & Lai

2001). Flat spacetime is presumed when tracking polarization (\mathcal{E}) and propagation (\mathbf{k}) vectors, since the general relativistic influences can be captured with single redshift and field distortion parameters that apply uniformly throughout the thin slabs at particular surface locales.

3.1 Photon Injection and Scattering

The initial injection of photons at the bottom of an atmospheric layer will often (but not always) be distributed isotropically in intensity, i.e. $I = (\text{const.})$. Assuming *flux isotropy*, the differential number of photons in an interval $(\theta, \theta + d\theta)$ in polar angle and $(\phi, \phi + d\phi)$ in azimuthal angle can be expressed as

$$\frac{dN}{d\theta d\phi} = f(\theta, \phi) = \frac{\mathcal{N}_i}{\pi} \cos \theta \sin \theta \quad . \quad (14)$$

Here the total number of photons \mathcal{N}_i passing through the surface where the injection occurs is obtained via an integration over all angles:

$$\int_0^{\pi/2} \int_0^{2\pi} f(\theta, \phi) d\theta d\phi = \mathcal{N}_i \quad . \quad (15)$$

The integration over θ spans the interval $[0, \pi/2]$ because we consider only the radiation emerging from the hemisphere below the injection surface.

To generate the initial propagation direction $\hat{\mathbf{k}}_0$ of photons at the base of the slab, the assumption of flux-weighted isotropy in Eq. (14) will be imposed in most of the illustrative results of Sec. 4. Thus, for a particular choice of polar coordinates specified relative to the z axis,

$$\hat{\mathbf{k}}_0 = (\sin \theta_0 \cos \phi_0, \sin \theta_0 \sin \phi_0, \cos \theta_0) \quad . \quad (16)$$

For this restrictive case of isotropy, the functional $f(\theta, \phi)$ applies, which is azimuthal symmetric. Therefore it is analytically invertible in both polar and azimuthal angles, yielding familiar forms expressed as functions of the two pertinent random variates, ξ_θ and ξ_ϕ :

$$\theta_0 = \frac{1}{2} \arccos(2\xi_\theta - 1) \quad , \quad \phi_0 = 2\pi\xi_\phi \quad . \quad (17)$$

This defines a uniform distribution weighted by the factor $\cos \theta_0$ that constitutes the angle-dependent flux of photons through the base of the slab. The factor of $1/2$ in the θ_0 formula is introduced to render it appropriate for injection in the upward hemisphere only. Therefore, two random number choices are required to specify the direction of the injected photon. In some of our high opacity simulation runs addressed in Section 5, the assumption of isotropy is relaxed via a routine adaptation of the injection algorithm.

The choice of polarizations for injected photons is not unique, and as will become apparent, the emergent polarization signatures for moderate opacity slabs will be dependent on the injection choice. In such circumstances, the scattering simulation will not yet have reached a truly Markovian domain. The only true zero polarization injection is to randomly select all components $\hat{\mathcal{E}}_\theta = \hat{\theta} \exp\{i\varphi_\theta\}$ and $\hat{\mathcal{E}}_\phi = \hat{\phi} \exp\{i\varphi_\phi\}$ both in vector direction $(\hat{\theta}, \hat{\phi})$ and in complex phase $(\varphi_\theta, \varphi_\phi)$, simultaneously isotropizing $\hat{\mathbf{k}}_0$. This then statistically generates zero for all the averages defining the Stokes parameters in Eq. (12), resulting in polarization isotropy on the Poincaré sphere.

The distance s a photon propagates between scatterings or before its first collision is determined probabilistically using the total cross section σ , which is a function of polarization $\hat{\mathcal{E}}_i$ and propagation vector \mathbf{k}_i : see Eq. (9). If the photon was initially at position \mathbf{r}_i , then the position at which it scatters is $\mathbf{r}_f = \mathbf{r}_i + s\hat{\mathbf{k}}_i$. For a *uniform* electron number density n_e , the propagation distance is sampled according to Poisson statistics:

$$\xi_s = \exp(-n_e\sigma s) \Leftrightarrow s = -\frac{\log \xi}{n_e\sigma}. \quad (18)$$

Accordingly, ξ_s is the random variate on the interval $[0, 1]$ that depends directly on the **optical depth** $\tau = n_e\sigma s$, yielding a mean free path $\lambda = 1/(n_e\sigma)$ for scattering. This form was actually used to compute the trajectories illustrated in Fig. 1. For non-uniform electron densities, this algorithm is easily adapted by working in optical depth space so that $n_e s$ is replaced by an integral of n_e over pathlength.

Once a scattering is determined to occur, the differential cross section must also be sampled probabilistically in order to determine the new propagation direction \mathbf{k}_f and polarization \mathcal{E}_f after scattering. This is accomplished by applying the *accept-reject method* to the suitably-normalized polarization-dependent differential cross section:

$$\begin{aligned} p(\xi_{\theta_f}, \xi_{\phi_f}) &\equiv \frac{8\pi}{3\sigma} \frac{d\sigma}{d\Omega_f} = \frac{\sigma_T}{\sigma} \frac{\mathcal{E}_f \cdot \mathcal{E}_f^*}{|\mathcal{E}_i|^2} \\ &\equiv \frac{(\hat{\mathbf{k}}_f \times \boldsymbol{\alpha}) \cdot (\hat{\mathbf{k}}_f \times \boldsymbol{\alpha}^*)}{\boldsymbol{\alpha} \cdot \boldsymbol{\alpha}^*} \end{aligned} \quad (19)$$

Here \mathcal{E}_f is calculated using Eq. (6), or equivalently, $\boldsymbol{\alpha}$ is formed using Eq. (4). Observe that both σ and $d\sigma/d\Omega$ are dependent on the initial polarization state and propagation direction. The form on the second line of Eq. (19) is obtained simply from the ratio of Eqs. (7) and (8), and so expressing its numerator using the Binet-Cauchy identity from vector analysis, it is quickly established that $0 \leq p(\xi_{\theta_f}, \xi_{\phi_f}) \leq 1$ for all possible $\hat{\mathbf{k}}_f$. Accordingly, $p(\xi_{\theta_f}, \xi_{\phi_f})$ is well posed for the accept-reject method on the unit cube, and it represents a scaled two-dimensional probability distribution in the variables θ_f and ϕ_f . We therefore employ two uniform and independent random variates ξ_{θ_f} and ξ_{ϕ_f} , identified with the values of $(1 - \cos\theta_f)/2$ and $\phi_f/2\pi$, respectively:

$$\theta_f = \arccos(2\xi_{\theta_f} - 1) \quad , \quad \phi_f = 2\pi\xi_{\phi_f} \quad . \quad (20)$$

The normalization condition for p can be written

$$\int_0^1 d\xi_{\theta_f} \int_0^1 d\xi_{\phi_f} p(\xi_{\theta_f}, \xi_{\phi_f}) = \frac{2}{3} \quad , \quad (21)$$

since $d\xi_{\theta_f} d\xi_{\phi_f} = d\Omega_f/4\pi$, and this gives an indication of good numerical efficiency of this protocol, given that the normalization is not much inferior to unity. The accept-reject method then selects an additional random variate ξ_p to represent the probability function p . Thus the three random numbers ξ_{θ_f} , ξ_{ϕ_f} , ξ_p identify a point P within a rectangular prism volume that is bifurcated by the $p(\xi_{\theta_f}, \xi_{\phi_f})$ surface. If P lies below the surface, then the values of ξ_{θ_f} and ξ_{ϕ_f} are accepted, and both \mathbf{k}_f and \mathcal{E}_f are then determined. If, however, the point P lies above the surface, then the selection is rejected, and the Monte Carlo decision process is initiated anew. In this way, on average, the differential cross section for scattering is sampled representatively by the volume beneath the surface.

4 ILLUSTRATIVE RESULTS AND CODE VALIDATION FOR MODERATE OPACITIES

This Section outlines some basic results from the polarized radiation transport simulation, and provides a level of validation via comparison with prior numerical analyses of the magnetic Thomson problem. Throughout, the magnetic field will be assumed uniform, though of different orientations with respect to the slab normal: see Fig. 1. The photons are monochromatic at select frequencies, and their injection is both isotropic and an unpolarized mix of linear polarization states. The zenith angle θ_z of the observer direction is a suitable choice for the polar angle of the anisotropic emergent radiation. The thickness of the slab will be specified via an optical depth parameter. Photons can exit either through the top of the slab at $z > h$, escaping to an observer at infinity with their Stokes parameter information being recorded, or through the bottom of the slab at $z < 0$, to be absorbed deep in the atmosphere. The loss of photons via absorption at $z < 0$ turns out to be quite significant at high optical depths, thereby limiting the computational efficiency of the simulation.

Results will be presented for two magnetic field orientations, along the local zenith and parallel to the slab surface. These cases bracket the range of possibilities on the neutron star surface, and one anticipates that as a neutron star rotates, the emergent polarization and intensity signals will be a pulsing mix of results from these examples and those pertaining to interstitial field orientations. The coordinate reference system will be chosen so that the Stokes U parameter is effectively zero, to within photon count statistics, with Stokes Q and V parameters being the depicted polarization measures. This simplification can be maintained for arbitrary magnetic colatitudes by orienting one Cartesian coordinate axis to coincide with a particular magnetic longitudinal plane. However, when extending to summing over different longitudes, U is no longer zero in general.

It is of interest to explore how the emergent Stokes measures vary with thickness/depth of the slab, and to assess at what thickness the scattering/diffusion is saturated, for which dependence on the photon injection angular and polarization distributions is minimal. There is no unique optical depth measure, since the scattering cross section depends on the photon energy. Here we will be guided by the choice of Whitney (1991a), centered on two preferred directions, namely parallel \parallel and perpendicular \perp to the slab's field direction. Note that these labels are below applied to optical depths and must be distinguished from the linear photon polarization state labels. For unpolarized (up) radiation, the scattering cross section in Eq. (52) in Appendix B yields optical depths parallel to and orthogonal to the field \mathbf{B} of

$$\begin{aligned} \tau_{\parallel} &= n_e h \sigma_{\text{up}}(\theta_i = 0^\circ) = \tau_T \frac{\omega^2(\omega^2 + \omega_B^2)}{(\omega^2 - \omega_B^2)^2} \quad , \\ \tau_{\perp} &= n_e h \sigma_{\text{up}}(\theta_i = 90^\circ) = \frac{\tau_T}{2} \left[1 + \frac{\omega^2(\omega^2 + \omega_B^2)}{(\omega^2 - \omega_B^2)^2} \right] \quad . \end{aligned} \quad (22)$$

These can be applied to any field orientation. Since the cross section is strongly frequency dependent, fixing the value of τ_{\parallel} or τ_{\perp} provides a useful path to comparing results for different frequencies. Accordingly, this parameter appears in the ensuing plots of this Section, as opposed to the familiar Thomson value $\tau_T = n_e h \sigma_T$. Furthermore, it enables direct

comparison with results from the Monte Carlo simulation of magnetic Thomson transport in Whitney (1991a,b).

While the framing of the discussion is centered on neutron star atmospheres, the results are also potentially applicable to dynamic hard X-ray bursts in magnetar magnetospheres, where the slabs can be considered to be localized portions of the outer layers of a Compton-thick cloud contained in closed field line regions. A caveat to this extension is that there are locales in the magnetosphere where the photon energy and the cyclotron energy exceed 20 keV and the magnetic Thomson restriction must be relaxed in favor of a full QED treatment. A second caveat is that the cold electron gas approximation must also be relinquished in order to accurately model magnetar bursts, thereby defining an extension that will be explored in future work.

4.1 The Polar Case

Fig. 2 displays the angular profiles of the emergent intensity distribution at the magnetic pole, where $\theta_z = 0^\circ$ is along the field, and the horizon direction $\theta_z = 90^\circ$ is perpendicular to \mathbf{B} . The distributions (linear scale) are integrated over azimuthal angles about the zenith, and assigned to bins of width 1° in θ_z . The normalization is determined by dividing by the total number of photons injected, which was $\mathcal{N}_i = 10^9$, and the escape probability from the slab is addressed in Fig. 4. Profiles are displayed for different slab thickness h using the optical depth parameter τ_{\parallel} as a proxy. The angle-integrated intensity generally declines monotonically with increasing τ_{\parallel} as the ability of photons to escape out of the top of the slab drops, and more photons cross the slab base into the stellar interior.

The distributions in Fig. 2 were generated using a flux-weighted isotropic injection of photons at the slab base, with equal numbers of linear polarizations \perp and \parallel chosen. The emergent distributions are sensitive to the injection choice. For example, the thesis results in Figs. 4.2 of Barchas (2017) illustrate how even with isotropic injection, the angular profiles depend on the specification of an unpolarized injection at the base, with isotropy of photon electric field vectors on the Poincaré sphere yielding different intensity (and polarization) distributions from the \perp / \parallel mode parity choice adopted here, and also a plasma eigenmode parity. The differences are substantial for thin slabs with $\tau_{\parallel} = 1, 2, 3$. Yet, the $\tau_{\parallel} \gtrsim 7$ examples correspond to circumstances where the radiative transfer has generally saturated in generating angular and polarization distributions. The shapes of the intensity profiles are then approximately independent of τ_{\parallel} and are only slightly sensitive to the injection choice; the exception to this is at low frequencies $\omega/\omega_B \lesssim 0.1$ and around the resonant frequency. We will expand upon this injection nuance in Section 5.

The six panels of Fig. 2 sample a representative array of photon frequencies/energies straddling the cyclotron frequency, thereby identifying a diversity of character for the angular profiles. In this sequence, the Thomson optical depth spans a wide range of values, with the $\omega = 0.99\omega_B$ example representing the resonant cyclotron case. While not depicted here, in all cases, the full angular distributions exhibited no dependence on the longitudinal angle (azimuth) within statistical precision. For $\omega/\omega_B \gg 1$, when the char-

acter approaches that of an unmagnetized plasma, the distributions possess a modest anisotropy in polar angle. In this domain, Eq. (22) indicates $\tau_{\parallel} \approx \tau_{\perp} \approx \tau_T$, yet the differential cross section contains anisotropy that permeates into the angular profiles realized in the radiative transfer. Remembering that these are intensity representations, they include a $1/\cos\theta_z$ flux weighting factor. Accordingly, the true light density anisotropy $n_{\gamma}(\theta_z, \phi_z)$ at the slab surface is proportional to $I \cos\theta_z$ and thus is skewed more markedly towards the field direction.

Below the cyclotron frequency, the anisotropy is more profound, evincing a strong collimation aligned with the magnetic field; note that the reduction in solid angle about \mathbf{B} imposes a modest decline very near $\theta_z = 0$. This collimation is the essence of the “pencil beam” distributions familiar in historic studies of accreting X-ray pulsars (e.g., Gnedin & Sunyaev 1974; Mészáros & Bonazzola 1981; Burnard, Arons & Klein 1991). For these $\tau_{\parallel} \leq 10$ examples, the origin of this collimation is mostly due to a high percentage of \parallel photons injected almost along \mathbf{B} emerging unscattered because of a markedly reduced cross section for these directions. This simulation bias is eliminated when the code is run in much higher opacity domains, and the beaming becomes much more muted, as will become apparent in Sec. 5. For the low frequency, modest opacity cases, the angle θ_p of the peak of the profile appears to correlate with frequency as $\theta_p \sim \omega/\omega_B$, a correlation that persists to lower frequencies than are exhibited here in supplemental runs performed for $0.025 \gtrsim \omega/\omega_B \gtrsim 0.01$. This coupling is naturally expected from the interplay between the incident photon angle and frequency present in the cross section for the \parallel polarization (ordinary) mode, an interplay illustrated in Fig. 10.

The intensity profile right in the cyclotron resonance is in striking contrast to those at other frequencies. Eq. (57) shows that relatively proximate to the cyclotron resonance, spanning $0.25 \lesssim \omega/\omega_B \lesssim 4$, scatterings into \parallel modes preferentially occur in the direction of \mathbf{B} . The \perp mode does not have this bias. Combined, they enhance the emergent intensity closer to the field direction i.e. for smaller zenith angles. The exception is right in the resonance, where the non-resonant contribution to $\parallel \rightarrow \parallel$ scatterings is generally negligible. The scatterings are then azimuthally symmetric, with a modest bias $\langle \sigma_{\perp} \rangle > \langle \sigma_{\parallel} \rangle$ in the angle-averaged cross sections; see Eq. (52) or Fig. 10. This makes for a generally broad distribution of photon zenith angles in density, that maps over to an intensity profile $I(\theta_z)$ that is moderately peaked near the horizon, $\theta_z = 90^\circ$ due to the flux weighting factor. This peaking is diminished by non-resonant $\parallel \rightarrow \parallel$ conversions that help drive the escape of light close to the field direction at other frequencies.

As a validation of the code, we can compare some of our angular distributions with those obtained in Whitney (1991a), who employed a different prescription for the magnetic Thomson cross section from the electric field vector formalism adopted here. Nevertheless, our code should reproduce Whitney’s anisotropies, and it does. Only limited direct comparison is possible, specifically exhibited here for frequencies $\omega/\omega_B = 0.25, 0.5, 2, 10$ and $\tau_{\parallel} = 7$. Data are actually taken from figures in Whitney’s thesis (Whitney 1989), being binned rather broadly ($\Delta\theta_z \sim 10^\circ$), limited by the computational statistics available at the time. Whitney’s intensity distributions for the magnetic pole are normalized

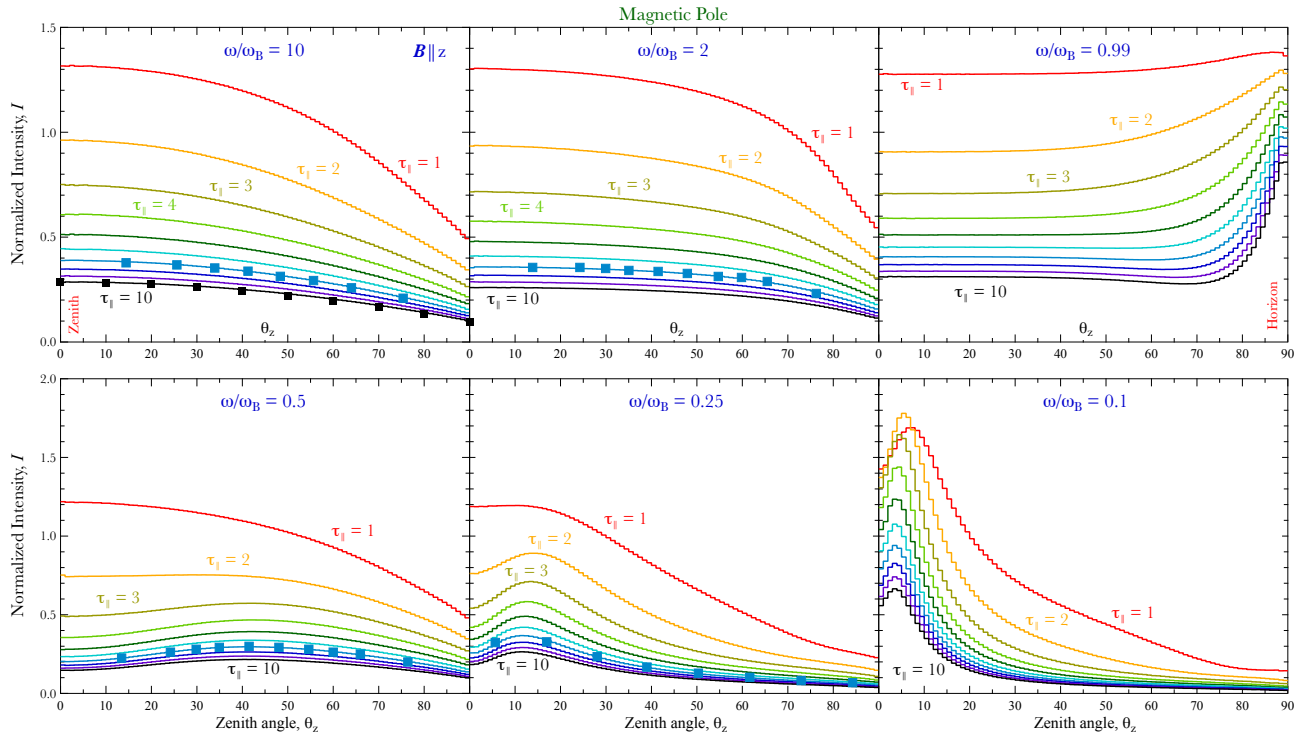


Figure 2. Angular distributions of intensity, as functions of the observer’s zenith angle θ_z , for the case of \mathbf{B} being in the zenith direction along the slab normal, appropriate to the magnetic pole. Each panel depicts results for one of six photon frequencies ω , specified in terms of the electron cyclotron frequency $\omega_B = eB/m_e c$. The colored histograms are for different optical depth parameters τ_{\parallel} , as defined in Eq. (22), ranging from $\tau_{\parallel} = 1$ (red) to $\tau_{\parallel} = 10$ (black), in unit increments; larger τ_{\parallel} incurring higher loss rates below the atmospheric slab into the stellar interior. The injection at the base of the slab was isotropic, with a net polarization of zero as a superposition of the \perp and \parallel linear polarization states with their particular Stokes parameters. The distributions are integrated over azimuthal angles about the zenith, so that they represent intensities captured in entire conical sectors of angular width $\Delta\theta_z = 1^\circ$. Simulation runs were for an injection of $\mathcal{N}_i = 10^9$ photons in all cases, except for $\omega/\omega_B = 0.1$, where $\mathcal{N}_i = 10^8$. Aqua squares for the $\omega/\omega_B = 0.25, 0.5, 2, 10$ examples represent data from simulations of Whitney (1991a); see text. The black squares for $\omega/\omega_B = 10$ are results adapted from Sunyaev & Titarchuk (1985) for non-magnetic Thomson transport, discussed in connection with Fig. 5 below.

in a particular fashion, and so are adjusted to approximately match the normalization generated here. Therefore, angular profile shapes are the available diagnostic, and the comparisons in Fig. 2 indicate strong agreement. Simulation results were also compared for other select ω/ω_B ratios adopted by Whitney (1989, 1991a), with comparable agreement, yet are not illustrated here. Whitney (1989) also produced an array of results for low optical depths $\tau_{\parallel} = 0.1$ that more directly capture the information imprinted by the scattering cross section. Angular profiles including polar plot diagrams were generated for $\tau_{\parallel} = 0.1$ cases using our code, and replicated results in Whitney (1989, 1991a) with good precision and without exception; again, these are not depicted here.

The polarization properties corresponding to five of these intensity panels are exhibited in Fig. 3, namely for $\omega/\omega_B = 0.25, 0.5, 0.99, 2, 10$, again with impressive statistics because the injection was for $\mathcal{N}_i = 10^9$ photons. These signatures are principally the Stokes Q (linear polarization) and V (circular polarization) parameters, both normalized to the emergent intensity I , as functions of observer zenith angle θ_z . At the right is the corresponding degree of polarization Π as defined in Eq. (10), and this trio displays a wealth of observational signatures. Statistically, U is essentially zero in the simulations for all θ_z bins other than the noisy 0° and 180° bins, which are subject to small number statistics. Accordingly, only two of the three polarization

quantities are independent. Approximate convergence of the polarization measures to fixed angular profiles is generally only realized for $\tau_{\parallel} \gtrsim 7$ in the examples shown. We note again that runs at $\omega/\omega_B \lesssim 0.2$ do not saturate at $\tau_{\parallel} = 10$ due to the large disparity in cross sections between the two linear polarization states. This occurs only for much larger values of τ_{\parallel} , for which run times increase dramatically. Note also that the results do not saturate for $\omega/\omega_B = 0.99$ at high zenith angles, in this case due to the complicated interplay of the circular polarization characteristics.

The coordinate choice combined with a viewing perspective in the general direction of \mathbf{B} dictate generally positive values for V/I . This follows from the general preponderance of circular polarization mode conversions $- \rightarrow +$ near to the field direction, inferred from Eq. (65), combined with $V > 0$ for $+$ helicity in these directions, deducible from the circular polarization eigenvectors in Eq. (60). A prominent feature of the plots is that substantial circular polarization emerges for $\omega/\omega_B \gtrsim 0.5$ when $\tau_{\parallel} = 10$, except when the viewing angle is orthogonal to the field (horizon). In particular, $|V/I|$ is maximized when looking along the field. This is expected since circular polarization states are the eigenmodes of propagation along the field in a magnetized plasma (e.g., Canuto et al. 1971). An accompanying signature is that the linear polarization $\Pi_{\text{lin}} \approx |Q/I|$ is zero along \mathbf{B} in general, and strong perpendicular to the field when either $\omega/\omega_B \gtrsim 0.5$ or $\omega/\omega_B \lesssim 0.25$. These proper-

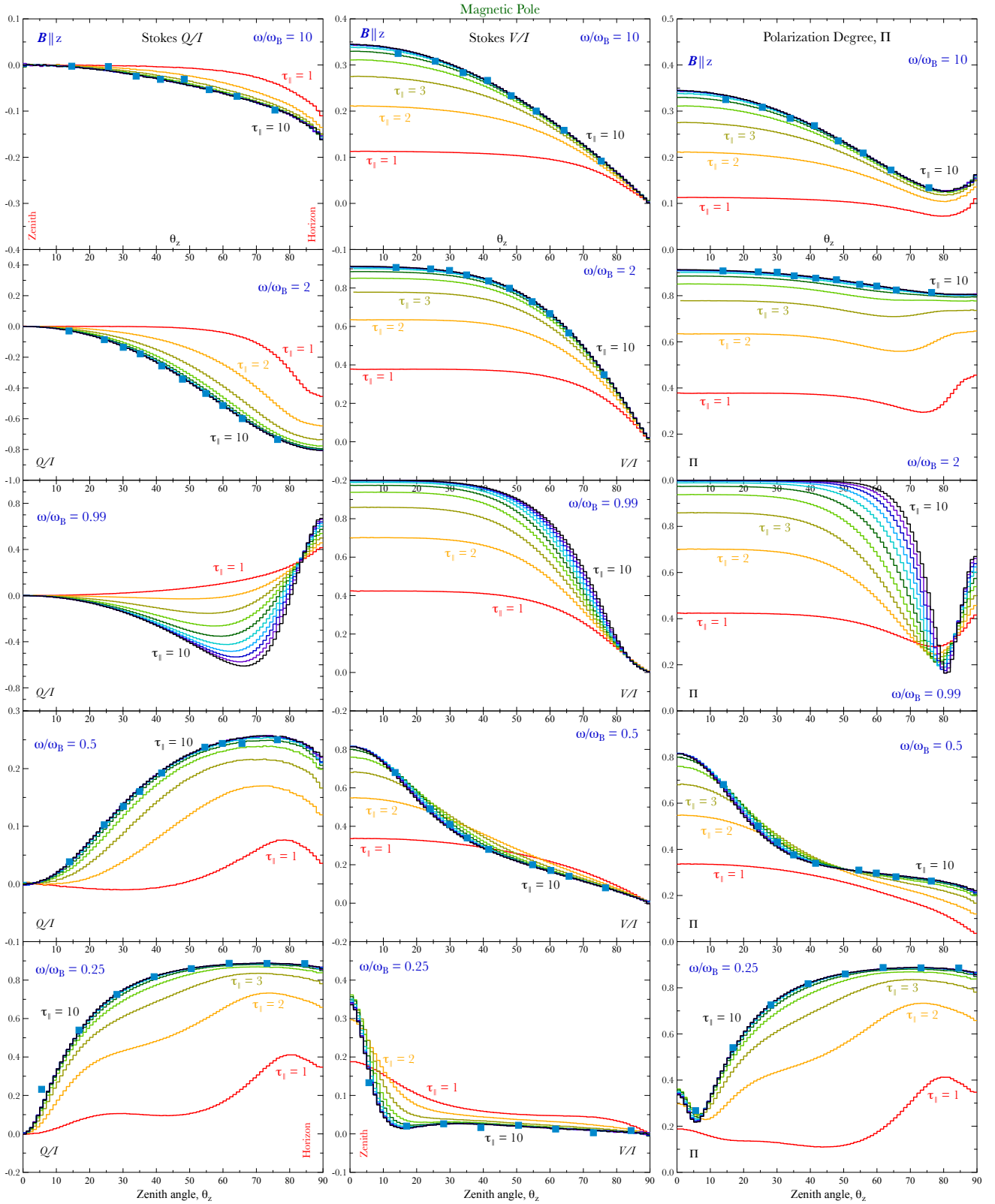


Figure 3. A companion plot for Fig. 2 generated using the same simulation runs. Angular distributions of Stokes parameters Q, V and the polarization degree Π , as functions of the observer’s zenith angle θ_z , again for the “polar” case of \mathbf{B} being in the zenith direction along the slab normal. Each row depicts results for one of five photon frequencies ω , specified in terms of the electron cyclotron frequency $\omega_B = eB/m_e c$. The colored histograms are for different optical depth parameters $\tau_{||}$, coded as in Fig. 2. The polarization angular profiles approximately saturate at large $\tau_{||}$. The injection at the base of the slab was isotropic and unpolarized as for Fig. 2. The distributions are again integrated over azimuthal angles about the zenith, applying to conical sectors of angular width $\Delta\theta_z = 1^\circ$. Simulation runs were for an injection of $N_i = 10^9$ photons. Aqua squares represent data from simulations of Whitney (1991); see text.

ties are direct consequences of the scattering cross sections, which evince strong circular polarization and small linear polarization along \mathbf{B} , with this bias reversed transverse to the field: see Eqs. (52) and (63) in Appendix B.

In terms of the variation with frequency, $|V/I|$ is generally quite large in the window $0.5 \lesssim \omega/\omega_B \lesssim 2$, straddling the cyclotron resonance. The origin of this is the comparative strength of the gyration motion of an electron induced by the incoming wave, so that the curl term in Eq. (4) contributes significantly to the overall value of α , i.e., the acceleration vector. A consequence of this is a relative balance between scatterings into the \perp and \parallel states, a balance maximized at $\omega/\omega_B = 1/\sqrt{3}$ that seeds $|Q/I|$ dropping to values below 0.3; see Fig. 10. At high frequencies $\omega/\omega_B \gtrsim 10$, the scattering is essentially non-magnetic and both the circular and linear polarization measures are smaller, on average. At small frequencies $\omega/\omega_B \lesssim 0.25$, the large disparity in opacities between these two linear polarization states yields a rapid rise in emergent $|Q/I|$ as ω declines. This is accompanied by a drop in the circular polarization that is retarded somewhat when viewing along \mathbf{B} , as exemplified in the $\omega/\omega_B = 0.25$ illustration. Also notable is that the sign of Q/I changes from negative to positive as the frequency drops through the cyclotron resonance, character persisting for all lower frequencies. This is a consequence of the frequency dependence of the balance between scatterings of \perp and \parallel states, which drives a change in the relative apportionment of polar $\hat{\mathcal{E}}_\theta$ and toroidal $\hat{\mathcal{E}}_\phi$ field components.

The polarization degree column of panels on the right of Fig. 3 reveals a rich behavior with both zenith angle and frequency that can afford significant diagnostic potential for X-ray polarimeters, which nominally are not expected to detect circular polarization, instead measuring Q, U and Π . Extremely strong Π emerges around the cyclotron frequency, near 100% for $\theta_z < 50^\circ$, and polarization degrees generally above 50% for sub-cyclotronic photon frequencies around $\omega \sim \omega_B/2$. In contrast, in the “non-magnetic domain” of $\omega/\omega_B = 10$, lower values of $0.2 \lesssim \Pi \lesssim 0.4$ result. The strong evolution of linear and total polarization degree in the frequency range straddling the cyclotron resonance signals the potential for these signatures to be powerful diagnostics on the emission environs in neutron stars of much lower magnetization than magnetars.

The last feature of Fig. 3 to note is the comparison of Q/I , V/I and Π with the results displayed in Whitney (1989). As with intensity, this was possible for $\tau_\parallel = 7$ and $\omega/\omega_B = 0.25, 0.5, 2, 10$, again revealing a satisfying agreement for all three polarization quantities. As noted above, the binning of Whitney’s data is coarse in zenith angle, dictated by statistics limited by the contemporaneous computational capability. Given that Whitney (1989, 1991a) modeled the magnetic Thomson transfer in a manner somewhat different from the electric field vector protocol here, using Jones matrix cross section evaluations, the favorable comparison of three Stokes quantities I, Q, V serves as an important code validation for the magnetic polar case. We note that insightful comparison with the Monte Carlo models of Fernández & Thompson (2007); Nobili et al. (2008); Fernández & Davis (2011) that treat scattering of linearly-polarized photons only in the cyclotron resonance is not possible.

4.2 Slab Escape Probabilities

The construction of these simulation runs guarantees a monotonic decline with τ_\parallel of the total numbers of photons escaping through the top of the slab. This naturally arises due to an increase in the cumulative probability that photons will diffuse deep into the interior of the atmosphere as net opacity increases, emerging from the bottom of the slab where they are injected. If one divides the intensities by the solid-angle-integrated net intensity, one arrives at the ratio of the number of photons \mathcal{N}_{esc} emerging from the top of the slab to the number \mathcal{N}_i injected at its base. This serves as a measure of efficiency of the simulation, i.e. the capturing of useful polarization data. This ratio $\mathcal{N}_{\text{esc}}/\mathcal{N}_i$, the outwards escape probability, is plotted in Fig. 4 as a function of the scaled photon frequency ω/ω_B , for the set of τ_\parallel values presented in the magnetic polar simulations in Figs. 2 and 3. This information is also presented there for the magnetic equator case that will be addressed in detail shortly.

The dots in this figure present results for runs with $\mathcal{N}_i = 10^9$ photons. A ubiquitous monotonic decline with τ_\parallel is apparent. For both polar and equatorial cases, the escape probability $\mathcal{N}_{\text{esc}}/\mathcal{N}_i$ varies with photon energy/frequency just as the differential cross section does. For the magnetic polar case on the left, the escape ratio peaks at the cyclotron frequency and is particularly low when $\omega \ll \omega_B$. The peaking is a consequence of the scattering cross section for the two linear polarization modes being similar at the cyclotron frequency, influenced also to some extent by the actual angular dependence of the differential cross section $d\sigma/d\Omega$. The number of scatterings per photon is still modest since scaling the runs by τ_\parallel essentially moderates the enhanced opacity at the cyclotron resonance. At highly-sub-cyclotronic frequencies, the scattering conversions $\perp \rightarrow \parallel$, while comparatively rare, do actually arise in the runs since fixing τ_\parallel as defined in Eq. (22) effectively guarantees them. Subsequently, $\parallel \rightarrow \parallel$ scatterings enhance and dominate the opacity, thereby biasing the escape of photons towards the lower boundary of the slab and reducing the $\mathcal{N}_{\text{esc}}/\mathcal{N}_i$ ratio.

For the magnetic equatorial case on the right of Fig. 4, for which we use τ_\perp as defined in Eq. (22) to tag the optical depth, the general dependence with frequency is quite different from that for the polar runs. Noticeably, the escape probability/efficiency increases in $\omega/\omega_B \ll 1$ domains. This too is a consequence of the action of prolific $\parallel \rightarrow \parallel$ scatterings subsequent to $\perp \rightarrow \parallel$ mode conversions. However, while the polar case samples escape somewhat aligned to the field direction, the equatorial case preferentially selects the complementary directions, those that are highly oblique to \mathbf{B} . Accordingly it captures the signals contributed by diffusion away from the field direction, and for $\omega/\omega_B \ll 1$ this constitutes considerably larger numbers of photons that underpin the inhibition of the $\mathcal{N}_{\text{esc}}/\mathcal{N}_i$ ratio when \mathbf{B} is along the zenith, i.e. for the polar case at left.

We remark that the detailed values of $\mathcal{N}_{\text{esc}}/\mathcal{N}_i$ will depend on the injection conditions, so that different values will be realized if the injection at the slab base is either anisotropic or polarized. Nonetheless, one may anticipate that the general shape of the escape probability curves will be somewhat similar to those depicted in Fig. 4.

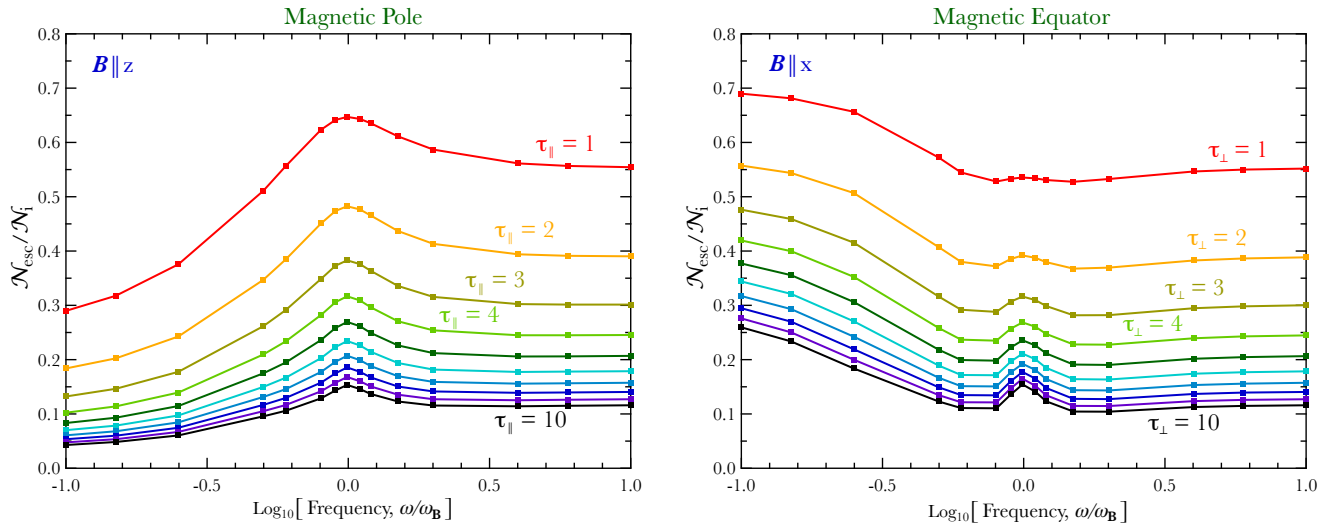


Figure 4. Outwards escape probabilities, $\mathcal{N}_{\text{esc}}/\mathcal{N}_i$, the ratios of the number of photons \mathcal{N}_{esc} emerging at the top of the slab to the number \mathcal{N}_i injected at its base. These are formed via integration over the angular distributions in Fig. 2. On the left is the magnetic polar case where the field is normal to the slab and in the zenith direction, and on the right is the magnetic equator case, for which \mathbf{B} is oriented parallel to the slab boundaries (horizon); these are respectively $\theta_B = 0$ and $\theta_B = \pi/2$ in Fig. 1. The dots at discrete frequencies represent data for runs with $\mathcal{N}_i = 10^9$ photons, and they are joined by straight lines to guide the eye. The expected monotonic decline of the escape probabilities with τ_{\parallel} and τ_{\perp} is obvious. The frequency dependence for the two cases is discussed in the text.

4.3 Equatorial Atmospheric Zones

The emission anisotropy and polarization characteristics depend strongly on the orientation of the magnetic field to the slab normal. To illustrate this and provide a contrast to the polar case in Sec. 4.1, an “equatorial” example with the field aligned parallel to the planar slab boundaries ($\theta_B = \pi/2$) is depicted in Fig. 5 (note that an intermediate $\theta_B = \pi/4$ case is explored in Barchas 2017). The simulations generating these distributions for $\theta_B = \pi/2$ also produced the escape probability results displayed on the right of Fig. 4. Since the distributions are integrated over the azimuthal angle ϕ_z about the zenith direction, the circular polarization V in this set-up is statistically equal to zero, and therefore is not displayed in the figure; non-zero V appears when particular ϕ_z values are selected. Since U is effectively zero due to the choice of coordinates, the Stokes parameter Q (center column) and polarization degree $\Pi \approx |Q/I|$ (right) in Fig. 5 provide essentially redundant representations of the same simulation output information for each ω/ω_B row.

The intensity profiles in the left column monotonically decline with increasing θ_z for all photon frequencies ω and optical depths τ_{\perp} . While this replicates the general behavior for $\omega/\omega_B > 1$ evident in Fig. 2, it differs vastly with the magnetic polar case at sub-cyclotronic frequencies $\omega/\omega_B < 1$. The reason for this disparity in character is simply that for this equatorial example, viewing angles generally do not coincide with the field direction and so the zenith azimuth ϕ_z integration acts to convolve information from the differential cross section at mostly large angles relative to the field direction \mathbf{B} . Geometrically, one can isolate photon directions almost parallel to the field by selecting particular ϕ_z azimuths with $\theta_z \sim 90^\circ$, and then the intensity profile does possess more variation with ω/ω_B , though generally the fluxes of photons emergent through the upper surface of the slab are then low since scattering into high θ_z directions is improbable, as is evident in the Figure’s intensity panels.

Thus, the intensity information in Fig. 5 can be described as essentially “non-magnetic” in character.

The top panel in Fig. 5 illustrates that the linear polarization Q/I is very small for zenith angles less than around 55° , and then increases somewhat as viewing angles more or less align with \mathbf{B} , but nevertheless remain small: $\Pi_{\text{max}} < 10\%$. This $\omega \gg \omega_B$ example is approximately a non-magnetic regime. An extensive analysis of polarization signatures from slabs for classical unmagnetized Thomson scattering was presented by Sunyaev & Titarchuk (1985), hereafter ST85, for the context of accretion disks near black holes. Fig. 4 of that paper indicates that for high optical depths, the intensity is maximized along the slab normal, and monotonically declines to around 1/3 of this maximum at the horizon. This is very close to the behavior exhibited here in the top left panel of Fig. 5, and also that for $\omega/\omega_B = 10$ in Fig. 2. The black squares exhibited in both the pertinent figure panels are data for the $\tau = 10$ curve illustrated in Fig. 4 of ST85, scaled by a constant factor so that the zero zenith angle values coincide with our simulation data. This excellent agreement with our $\tau_{\perp} = 10$ results when $\omega \gg \omega_B$ is expected since then the magnetic differential cross section in Eq. (48) approaches the familiar non-magnetic one.

Turning now to the polarization comparison, Fig. 5 of ST85 demonstrates that in the absence of a magnetic field, when $\tau = 10$ the linear polarization degree is zero along the slab normal, and rises monotonically to a value of around 11-12% when viewing almost along the surface. While this Π_{max} maximum is somewhat higher than the $\tau_{\perp} = 10$ magnetic equatorial result at $\theta_z = 90^\circ$ in Fig. 5, it is somewhat lower than the polar Π_{max} value along the horizon in Fig. 3, where $V = 0$ and the signal is linearly polarized; the average of our polar and equatorial evaluations is within around 9% of the ST85 value at $\theta_z = 90^\circ$. Moreover, for intermediate zenith angles, $50 < \theta_z < 90^\circ$ the linear polarization degrees at $\tau = 10$ from the Sunyaev & Titarchuk (1985)

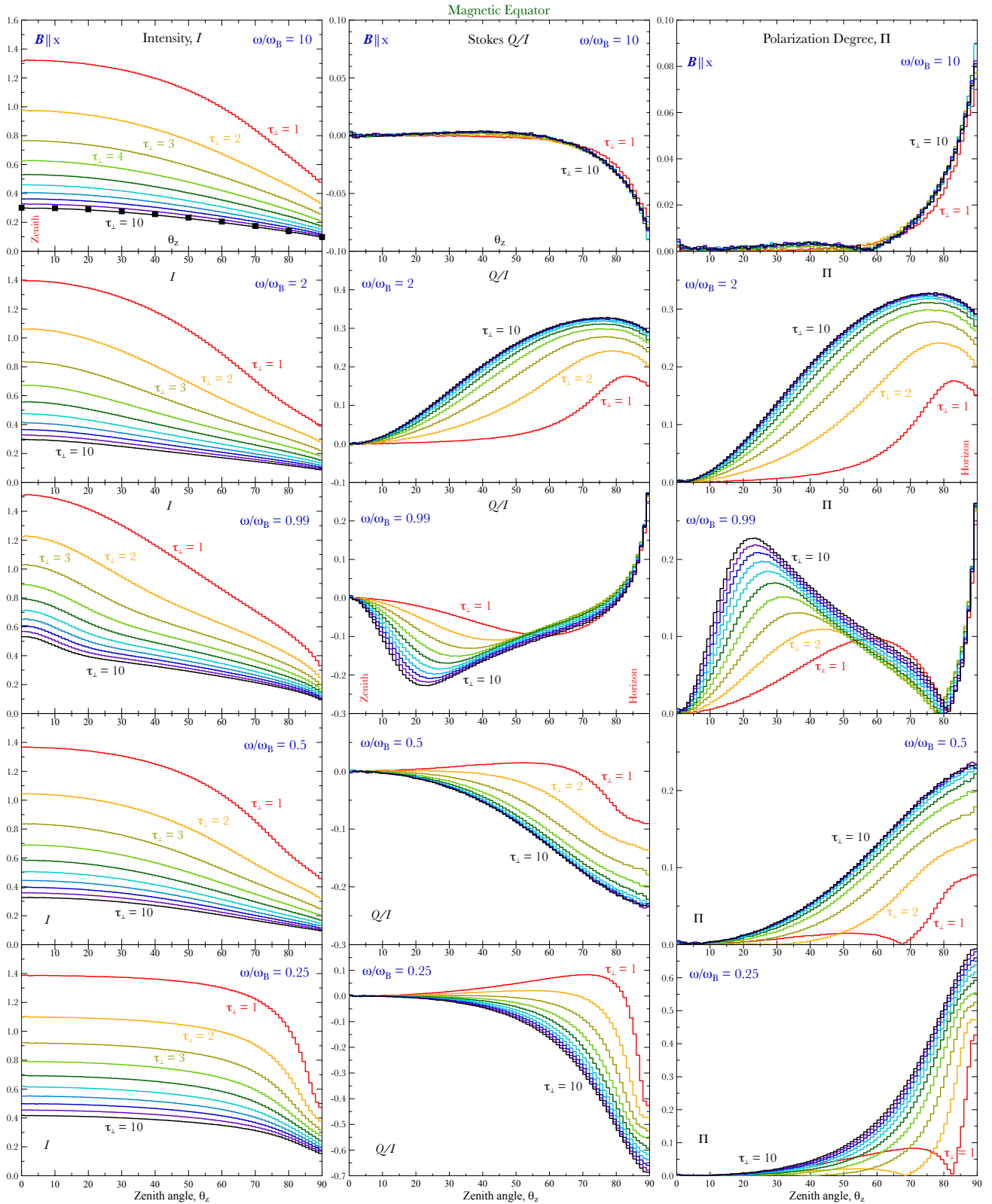


Figure 5. Angular distributions for intensity I , Stokes parameter Q and the polarization degree Π , as functions of the observer’s zenith angle θ_z , now for the “equatorial” case of \mathbf{B} being parallel to the slab surface. Each row depicts results for one of five photon frequencies ω , specified in terms of the electron cyclotron frequency $\omega_B = eB/m_e c$. The colored histograms are for different optical depth parameters τ_{\perp} , as defined in Eq. (22). The angular profiles approximately saturate at large τ_{\perp} . The injection at the base of the slab was isotropic and unpolarized as for the polar case. The distributions are again integrated over azimuthal angles about the zenith, applying to conical sectors of angular width $\Delta\theta_z = 1^\circ$. Simulation runs were for an injection of $\mathcal{N}_i = 10^9$ photons. The black squares for $\omega/\omega_B = 10$ are intensity results (suitably scaled) from Sunyaev & Titarchuk (1985) for non-magnetic Thomson transport.

figure consistently lie between our polar and equatorial simulation values for $|Q/I|$, all exhibiting the same monotonic increase with θ_z towards the slab horizon.

A material difference between our results and the non-magnetic ones of Sunyaev & Titarchuk (1985) is that here there is significant emergent circular polarization V/I when \mathbf{B} is not aligned parallel to the slab surface. A consequence of resonant circulation of the scattering electron, this non-zero V/I bolsters the net polarization degree signal and introduces departures from monotonic trends of Π with θ_z : see Fig. 3. Inspection of the two directional opacity measures in Eq. (22) indicates departures from the Thomson value τ_T by 1.5–3% at $\omega = 10\omega_B$, so that magnetic influences are still present. A more precise comparison between the magnetic Comptonization polarization results here and the non-magnetic analog in ST85 is thus best performed at higher frequencies. Accordingly, we ran simulations in both polar and equatorial cases for $\omega/\omega_B = 10^2$, and found excellent agreement between our angular distributions for intensity and $\Pi_{\text{lin}} \equiv |Q/I|$ at $\tau_{\perp} = 10$ and the $\tau = 10$ ones in Figs. 4 and 5 of ST85. We also observed that in the polar case, $|V/I| < 0.04$ at this much higher frequency, a consequence of the two circular polarization cross sections coalescing when $\omega \gg \omega_B$: see Eq. (63) in Appendix B.

For the more magnetic equatorial cases with $\omega/\omega_B \leq 2$, the intensity profiles at $\tau_{\perp} = 10$ largely resemble those at super-cyclotronic frequencies in the polar examples of Fig. 2. This again is due to the higher zenith (horizon) emergences requiring a last scattering very near the slab surface, an improbable occurrence. The zenith angle distributions for Stokes Q for the horizon field orientation look very different from those of the polar case. Their relative behavior is ascribed to the fact that the polar and equatorial cases preferentially sample complementary perspectives relative to the field direction at any chosen zenith angle. The Q/I values at $\omega/\omega_B = 2, 0.5, 0.25$ in Figs. 3 and 5 are of opposite sign, and so if one sums them, relatively small net Q/I results, albeit not exactly zero. Intuitively one expects zero net linear polarization from an isotropic superposition of magnetic field orientations, and the combination of the polar and equatorial configurations is the first stage of constructing such a superposition. The exception to this ‘‘cancellation’’ is provided by the resonant case $\omega/\omega_B = 0.99$, where the scattering angle summations conspire to give mostly negative Q/I at $\theta_z < 80^\circ$ for both polar and equatorial field orientations, and positive Q/I for near-horizon viewing.

A nuance that needs brief attention concerns the co-adding of the polarization information from all slab exit azimuths ϕ_z for the illustrations of this Section. For the polar case in Fig. 3, results from all ϕ_z are statistically identical due to the azimuthal symmetry, so the addition just improves the simulation data statistics. In contrast, for non-zenith field orientations such as for the equatorial depictions in Fig. 5, the Stokes I, Q, V vary with azimuth ϕ_z and so the summations represent a mixing of azimuthal information. Note that for a particular observer detecting photons from a particular point on the stellar surface, individual values of *both* θ_z and ϕ_z are selected for a particular ray propagating in curved spacetime to infinity.

A comparison of our equatorial slab results with those from the same field orientation in Whitney (1991b) is not as straightforward as for the polar field case, since she pre-

sented distributions for particular azimuths ϕ_z . In doing so, we focus on $\omega/\omega_B = 0.5, 0.25$ values, for which Whitney presented results in Figs. 5 and 6 of her paper, respectively. Therein, she selected azimuthal angles $\phi_z = 0^\circ, 90^\circ, 180^\circ$ to present her results. It was not clear what ranges of ϕ_z these constituted. Nor is it apparent what injection distribution of angles and polarizations of photons were assumed in Whitney (1991b). Since the results presented therein were for a low opacity, $\tau_{\perp} = 3$, the Stokes parameter signals are generally sensitive to the injection information; this was evident in our various exploratory simulation runs. It was also unclear what was the statistical quality of the results presented in Figs. 5 and 6 of Whitney (1991b), no doubt diminished by the sub-selection of particular azimuths, and muting details through coarse θ_z binning.

To best approximate her cases, we collected subsets of the data presented for the $\mathcal{N} = 10^9$ runs in Fig. 5 with unpolarized and isotropic injection, binned in azimuthal ranges of 10° that were centered on $\phi_z = 0^\circ$ and $\phi_z = 90^\circ$; note that $\phi_z = 180^\circ$ provides redundant information in relation to the $\phi_z = 0^\circ$ case. Comparing our $\omega/\omega_B = 0.5$ distributions with Fig. 5 of Whitney (1991b), we find good general agreement for both $\phi_z = 0^\circ$ and $\phi_z = 90^\circ$ between her and our distributions of intensity, V/I and effective linear polarization degree $\Pi_{\text{lin}} \approx |Q/I|$ throughout the zenith angle range $0 < \theta_z < 90^\circ$. Note again that $U/I \approx 0$ in this field configuration. Comparing our $\omega/\omega_B = 0.25$ distributions with Whitney’s Fig. 6, the agreement was just as good for both V/I and Π_{lin} , for both azimuths $\phi_z = 0^\circ, 90^\circ$, and also for the intensity for $\phi_z = 90^\circ$. However, significant deviations at the 10–30% level arose for zenith angles $50^\circ < \theta_z < 80^\circ$ for the $\phi_z = 0^\circ$ intensity. In the absence of sufficient detail concerning the photon injection and data binning in Whitney (1991b), it is not possible to isolate possible causes for the origin of these differences.

5 POLARIZATION AT HIGH OPACITIES

In order to move beyond the testing and validation phase, in preparation for the implementation of the radiation transport code in more sophisticated models of neutron star atmospheres, it is necessary to explore the polarization characteristics of magnetic Thomson transport in high opacity domains. This is suitably done by shedding the simulations of the slab geometry and just recording angular distributions of photon number and polarization measures subsequent to large numbers of scatterings. Accordingly, the ensuing results will not at first be applied specifically to any particular neutron star locale, but will be broadly representative of characteristics deep in atmospheric slabs. These results are just functions of the angle θ between the ultimate photon momentum \mathbf{k} and magnetic field \mathbf{B} vectors, and the scaled photon frequency ω/ω_B ; it will emerge that a set of quite simple empirical approximations can encapsulate the Stokes parameter dependences on θ and frequency. These will then be employed to simulate high opacity slab results for polar locales in Section 5.4, an extension that enables modeling of thicker regions than was possible in Whitney (1991a,b). This paves the way for precision simulation of optically thick photospheres, whether they belong to neutron star/magnetar surface layers, accretion columns or magnetar burst regions.

5.1 High Opacity Radiation Transfer Simulations

The simulation uses an isotropic injection at a single point, but omits a flux weighting analogous to that in Eq. (17). The injection is also unpolarized, employing an equal mix of linearly-polarized \parallel or \perp photons in the choice of the complex electric field vectors; see Eq. (50). Specific angular and polarization information at injection is irrelevant to the simulation output in this Markovian setup. Photon frequencies are selected from a uniform distribution in $\log_{10}(\omega/\omega_B)$. To generate excellent statistics, $\mathcal{N}_i = 10^9$ photons were distributed in the frequency, angle and polarization variates. Their paths were followed for exactly $n = 100$ magnetic Thomson scatterings, and then their final direction and polarization information were recorded, regardless of their final location relative to the injection point. The choice of 100 scatterings was sufficient to generate a Markovian scattering sequence and sample the differential cross section with sufficient density in polar (θ) and azimuthal (ϕ) angles. We tested this by performing simulations with 10^3 and 10^4 scatterings, but with somewhat fewer injected photons, and observed no material differences within statistics (e.g. see Fig. 2.6 of Barchas 2017).

At the outset, a photon is assigned to one of 160 logarithmic frequency bins, uniformly sized in $\chi \equiv \log_{10}(\omega/\omega_B)$. After a scattering sequence is complete, the photon direction is recorded in one of 120 angle cosine bins, uniformly sized in $\mu = \cos\theta$. Since the differential cross section is dependent only on the difference ϕ_{fi} in azimuths (e.g. see Eq. (57) for linear polarizations), the resultant distributions are independent of azimuth ϕ , and so are co-added. Photon number count and Stokes \hat{Q} and Stokes \hat{V} thereby generate three data arrays, along with a derivative fourth array specifying Π . The number count generates a photon number angular distribution $A_\omega(\mu)$ (a scaled intensity) that will be termed the **re-distribution anisotropy** as it specifies the terminal anisotropy at high opacity when re-distributing angles and polarizations through Thomson scattering; it is normalized to one injected photon:

$$\int_{-1}^1 A_\omega(\mu) d\mu = 1 \quad . \quad (23)$$

If one uniformly distributes a large number of injection locales in space, the cumulative output count distribution in μ would remain statistically the same. Therefore, $A_\omega(\mu) \propto I(\mu) \propto n_\gamma(\mu)$ represents a scaling of the intensity $I(\mu)$ in the direction of \mathbf{k} or the total density $n_\gamma(\mu)$ contributed by the different polarizations. The proportionality coefficient $A_\omega(\mu)/I(\mu)$ is actually a function of μ , as will be detailed with the interpretation of $A_\omega(\mu)$ in Section 5.3. Since this scaling applies to all Stokes parameters, it drops out when forming the ratios $\hat{Q} = Q/I$ and $\hat{V} = V/I$, a convenient circumstance in the ensuing exposition of results.

To explore the connection between the data output and photon diffusion, experiments were performed where the position (x_n, y_n, z_n) of a photon after the final (n^{th}) scattering was recorded, and collected to form statistical averages of the diffusion process. Here the z -direction is aligned with \mathbf{B} , and (x, y) are Cartesian coordinates in the orthogonal plane. The diffusion “step” is nominally the mean free path $\lambda = 1/[n_e\sigma(\mu)]$ for scattering, and is anisotropic and polarization dependent. Units of $n_e = 1 = \sigma_T$ were chosen for

expediency. The total number of scatterings was increased to $n = 10^3$, and once n exceeded around 10, the expected correlations $\langle x_n^2 + y_n^2 \rangle \propto n$ and $\langle z_n^2 \rangle \propto n$ were demonstrated to impressive statistical precision. The ratio of these two diffusion coefficients, i.e., $\langle x_n^2 + y_n^2 \rangle / \langle z_n^2 \rangle$ was generally between 1 and 2, marking the anisotropy of magnetic Thomson diffusion. In general, this ratio was frequency-dependent, and for $\omega/\omega_B = 30$ its numerical value was 2.01, signalling isotropic diffusion in a non-magnetic domain.

The information from these high opacity runs is presented as *frequency-angle maps* in Fig. 6, with the individual legends defining the color scales for anisotropy A_ω , Q/I , V/I and total polarization Π . With the binning described just above, the raw data that these panels represent would appear more pixellated than is displayed. To make for a smoother depiction, we employed the Mathematica built-in **Interpolation** function with its **Spline** option (the default setting of the order is 3, i.e. cubic) to obtain the photon number and Stokes parameters as more continuous functions of μ and χ . The smoothing corresponds to 360 μ and 320 χ bins, both spanning the interval $[-1, 1]$, so that the map pixellation is six times denser than the original data. This protocol does not change the information conveyed, and we tested this with runs employing refined binning that were subject to poorer statistics, and found no conflicts. The photon number density is normalized so that for each frequency the integral of photon number over μ equals unity.

A synopsis of the general character of the frequency-angle maps is as follows. The angular distribution $A_\omega(\mu)$ is fairly isotropic at high frequencies in the quasi-non-magnetic domain, and then becomes peaked along and anti-parallel to the field as the frequency drops and transitions through the cyclotron frequency. This alignment of beaming with the field direction is driven by the general preponderance of scatterings that generate small θ_f , as is evident in Eq. (57). When $\omega/\omega_B \sim 1/\sqrt{3}$, corresponding to approximate equality of cross sections for the two linear polarizations, there is an abrupt transition to a domain where the density is much greater perpendicular to the field. Then, most of the scatterings are non-resonant $\parallel \rightarrow \parallel$ events, biasing the population to a predominance of $\pi/4 \lesssim \theta_f \leq \pi/2$ final angles, with occasional $\parallel \rightarrow \perp$ conversions; again see Eq. (57). Since we used 160 frequency bins, the number of photons for each frequency was 6.25×10^6 . Thus while the runs that generated Fig. 6 persisted only for 100 scatterings per photon, so that $\parallel \rightarrow \perp$ conversions might occur with a probability of 0.1–1 for each injected photon, there were enough conversions in the ensemble to realize reasonable statistics in the various distributions. Inverse conversions $\perp \rightarrow \parallel$ possessed similar occurrence probabilities; see Eq. (59).

The Stokes Q/I is generally of a small value at $\omega/\omega_B \sim 10$, and becomes more negative when transitioning through the resonance. Again, an abrupt change in character arises at $\omega/\omega_B \sim 1/\sqrt{3}$, below which Q/I is positive. This bifurcation is a direct consequence of the relative values of the cross sections in Eq. (59). Above $\omega/\omega_B = 1/\sqrt{3}$, since small θ_i are favored, polarization conversions $\parallel \rightarrow \perp$ are more prevalent than $\perp \rightarrow \parallel$ ones, so the \perp state emerges as the dominant linear polarization, yielding $Q < 0$. The balance is inverted below $\omega/\omega_B = 1/\sqrt{3}$ and then the \parallel mode is more prevalent and $Q > 0$. If one inserts the linear polarization modes in Eq. (50) into the Stokes vector definitions in

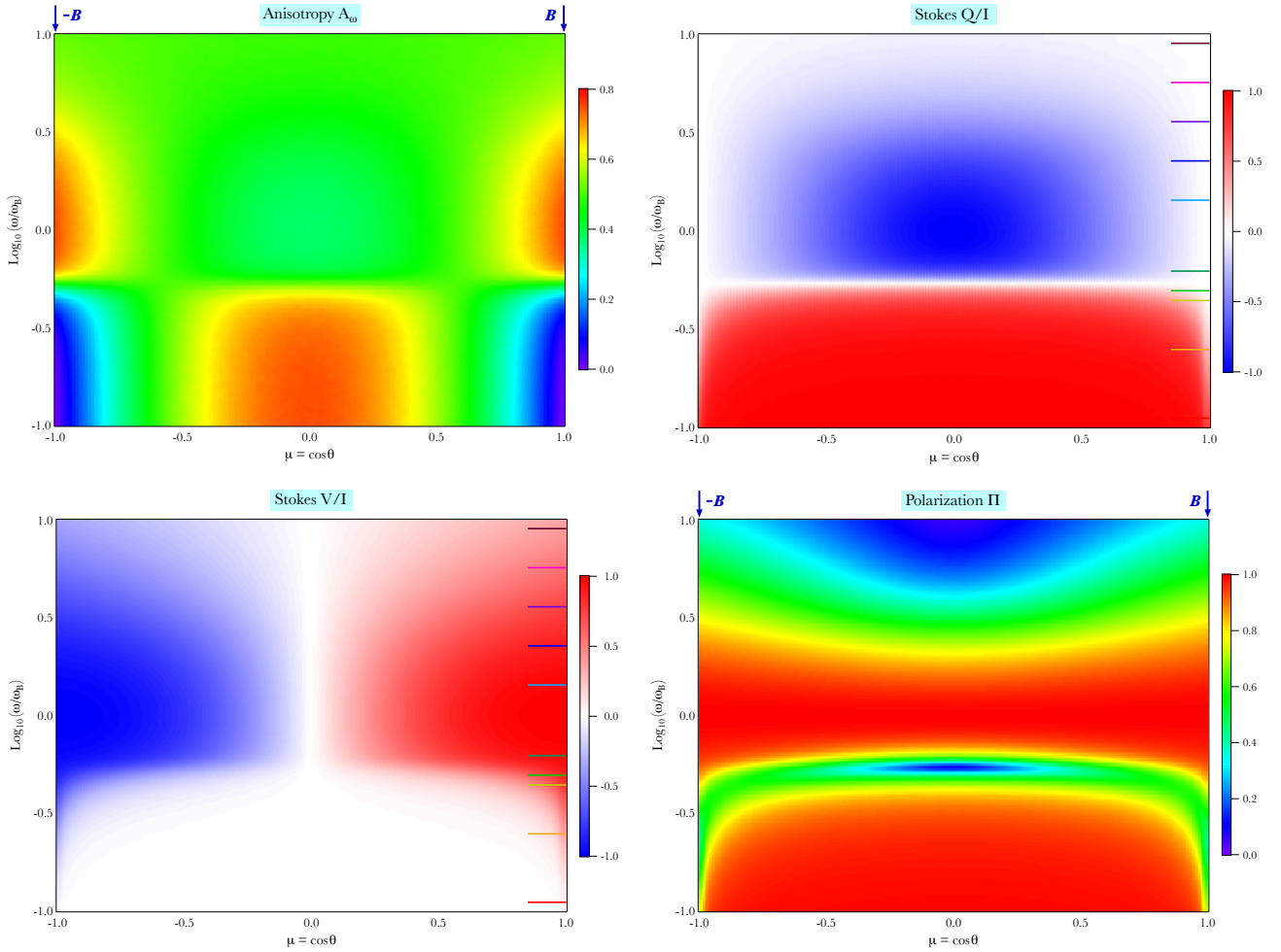


Figure 6. Maps of the angular distributions for the re-distribution anisotropy A_ω , Stokes parameters Q/I , V/I and the *total* polarization degree Π as functions of photon frequency (log scale on the ordinate). The angle θ is measured relative to the magnetic field direction, which is indicated in the A and Π panels, with the abscissa expressing the cosine $\mu = \cos\theta$. The Stokes parameters were recorded after exactly 100 scattering events for each photon, with the injected photons sampling isotropic and unpolarized distributions, for a total of $N_i = 10^9$ photons. The injection was also uniformly distributed in $\chi = \log_{10}(\omega/\omega_B)$ among 160 frequency bins. Short horizontal lines in the Q and V maps display the frequencies selected to compare with empirical approximations in Fig. 7.

Eq. (12) one quickly infers that for $\phi = 0$ (i.e., the observer plane), that $\hat{Q}_\perp = -1$ and $\hat{Q}_\parallel = 1$. This establishes the simple interpretation that $Q < 0$ signals a preponderance of \perp polarization, while $Q > 0$ marks a dominance of \parallel modes. The angular dependence of Q/I is generally significant, and will be highlighted shortly.

In terms of the circular polarization, V/I is small below the “equipartition frequency” $\omega = \omega_B/\sqrt{3}$ as the circularity $\Delta_B(\omega)$ in Eq. (64) becomes small in this domain. At resonant and higher frequencies, V/I is significant up to $\omega/\omega_B = 10$ because of the strong circularity imposed by the electron gyration in the scatterings. By inspection of the circular polarization “mode-switching” differential cross section in Eq. (65) in Appendix B, when $0 < \theta_f < \theta_i$ in a scattering, the production of the $+$ polarization is favored over the generation of the $-$ state, leading to generally positive V when $0 < \theta < \pi/2$, as is observed in Fig. 6. Note that V/I is naturally odd in the angle cosine μ , with the prevailing helicity depending on the direction of propagation $\hat{\mathbf{k}}$ relative to that gyration, and therefore $\hat{\mathbf{B}}$.

The information in Fig. 6 is inherently different from

that in the slab transport displays of Figures 2, 3 and 5. It defines the approximate asymptotic solution to the radiative transfer angular and polarization re-distribution problem for an infinite medium. It was derived in the absence of boundaries that define angle-dependent and polarization-dependent escape probabilities, and thereby omits their critical influences. For example, contributions to the intensities near the zenith in Fig. 2 sample small solid angles and therefore are statistically improbable. At the same time, intensity contributions for $\theta_z \sim 90^\circ$ near the slab horizon may sample large solid angles, yet they require that the last scattering occur very near the slab surface, again an improbable circumstance. These modify the emergent angular distributions of intensity relative to those in Fig. 6 that constitute regions deep down in the denser portions of an atmospheric slab. Similar biases arise for the polarization Stokes parameters Q and V when considering slab geometry. We remark that while the results depicted in Fig. 6 were produced using a homogeneous medium, they apply regardless of density stratification along $\hat{\mathbf{B}}$, which just acts to generate a gradient in scattering scale-lengths along the field.

5.2 Empirical Approximations in μ and ω

The symmetry with respect to the polar angle cosine μ of the maps in Figure 6 suggests a simple mathematical dependence. This is borne out with empirical fits to the data at a variety of frequencies that are addressed here. The origin of this simplicity is in the quadratic μ dependence of the differential cross sections for linear and circular polarization scatterings presented in Appendix B, and will be discussed in Section 5.3. For a large number of scatterings where the configuration is not changed by the action of scattering, one therefore anticipates that the photon re-distribution anisotropy assumes the form $A_\omega(\mu) \propto 1 + \mathcal{A}(\omega)\mu^2$. The evenness in μ , obvious in Figure 6, is driven by the same property of the total cross section $\sigma(\mu)$. Adhering to the normalization in Eq. (23), the form

$$A_\omega(\mu) = \frac{3}{2} \frac{1 + \mathcal{A}(\omega)\mu^2}{3 + \mathcal{A}(\omega)} \quad , \quad (24)$$

emerges. Observe that this function is identically equal to $1/2$ for all frequencies when $\mu = \pm 1/\sqrt{3}$; this is just a consequence of the Legendre 2-point quadrature evaluation of the integrals in the radiation transport formalism.

To highlight the symmetries of the frequency-angle maps, we formed horizontal sections of them at select frequencies identified by the markers along the right axes of the Q/I and V/I panels in Fig. 6. The data for these frequencies were presented as the ‘‘curves’’ with discrete points in Fig. 7, employing the same color coding as the markers in Fig. 6. In the case of $A_\omega(\mu)$ depicted in the left panel, the coefficient $\mathcal{A}(\omega)$ was determined numerically by fitting the data at each of these selected frequencies plus about another dozen more (not displayed). The result was a data ‘‘curve’’ in frequency space that was then fit by an empirical function of ω/ω_B . This fitting protocol was most conveniently detailed using the variables

$$\psi = 16\chi^2 \quad , \quad \chi = \log_{10}(\omega/\omega_B) \quad . \quad (25)$$

The resulting frequency function for the anisotropy fits was determined on the range $-1 \leq \chi \leq 1$ to be

$$\mathcal{A}(\omega) = \begin{cases} \frac{2 - \psi/10 - 12\psi^2/11 + 24\psi^3/19}{1 + 4\psi^5/5} - 1, & \omega < \omega_B, \\ \frac{1 - 5\psi/38 + 17\psi^2/1840 - \psi^3/4250}{1 + \psi^2/80}, & \omega \geq \omega_B. \end{cases} \quad (26)$$

This is an empirical form suitably compact for numerical applications. It possesses a signature value of $\mathcal{A}(\omega) = 1$ at the cyclotron resonance, where $A_\omega(\mu) = 3(1 + \mu^2)/8$. In the magnetar surface X-ray domain where $\omega/\omega_B \ll 1$, $\mathcal{A}(\omega) \approx -1$ and $A_\omega(\mu) \approx 3(1 - \mu^2)/4$, so that photon propagation is clearly suppressed along or anti-parallel to \mathbf{B} . Also, $\mathcal{A}(\omega)$ approaches zero when $\chi = +1$ in the quasi-non-magnetic domain, so that then $A_\omega(\mu) \approx 1/2$ and the photons are almost isotropic. Outside the interval $-1 \leq \chi \leq 1$, the $\chi = \pm 1$ endpoint values for \mathcal{A} can be adopted. We note that a full phase matrix analysis of the radiative transfer would not generate this mathematical form, instead capturing the analytics of the differential cross section, yet it may in principal be more complicated; its determination is deferred to a future investigation.

The analytic approximation for the anisotropy formed by the combination of Eqs. (24) and (26) is represented as the solid curves in the left panel of Fig. 7 for the selected frequencies. The precision of its fit to the simulation data points is better than 2%, instilling confidence in its utility.

The linear and circular polarization data were subjected to fitting protocols similar to the anisotropy ones. Since linear polarization is zero for propagation in either direction parallel to the field, one anticipates that $Q \propto 1 - \mu^2$. In forming the Q/I ratio, the quadratic dependence of the anisotropy appears in the denominator, so that the fit should be a Pad e approximant in μ . Guided by this, we arrived at a linear polarization empirical fit defined by

$$\frac{Q_P}{I_P} \equiv \hat{Q}_\omega(\mu) = \frac{\mathcal{A}(\omega) [\mu^2 - 1]}{1 + \mathcal{A}(\omega)\mu^2} \quad . \quad (27)$$

We have now introduced $I_P \propto A_\omega$ anticipating the phase matrix interpretation of this anisotropy in Section 5.3, and its Stokes counterparts Q_P and V_P . Note that the frequency dependence of the numerator is just that for the anisotropy, as opposed to some other function of ω . This is not a coincidence, and should emerge from a full polarization phase matrix analysis of the transport; this effective coupling between I and Q is apparent in the Stokes parameter form of the cross section in Eq. (13).

The circular polarization is necessarily odd in μ due to this parity property of the cross section: see Eq. (63). The obtained fitting function was

$$\frac{V_P}{I_P} \equiv \hat{V}_\omega(\mu) = \frac{2\mathcal{C}(\omega)\mu}{1 + \mathcal{A}(\omega)\mu^2} \quad , \quad (28)$$

for

$$\mathcal{C}(\omega) = \begin{cases} \frac{1 - 7\psi/25 + 9\psi^2/25 - \psi^3/59}{1 + \psi^{3.8}}, & \omega < \omega_B, \\ \frac{1 - \psi/90}{1 + 3\psi^{1.2}/25}, & \omega \geq \omega_B. \end{cases} \quad (29)$$

This function, which applies to the domain $-1 \leq \chi \leq 1$, appears because the circularity of the polarized transfer inherently differs from its linearity, whether proximate to the cyclotron resonance or not. Signature values are $\mathcal{C}(\omega) = 1$ at the cyclotron resonance, $\chi = 0$, and it is very close to zero when $\chi = -1$. When $\chi = +1$ is around 0.19, and does approach zero for $\omega \gg \omega_B$, albeit somewhat slowly.

Having assembled these empirical fits to the frequency-dependent anisotropy and Stokes parameters, numerical checks on their validity are in order. The high opacity simulation was run again, but with Eqs. (24–29) used to provide an alternative, polarized injection (see below). For $n = 100$ scatterings for each photon, the subsequent results were indistinguishable from Fig. 6. Yet this provides a Markovian test that is not an incisive probe. We therefore performed such a simulation for just $n = 1$ scattering, and the results in Figs. 6 and 7 were reproduced with excellent precision. This validation demonstrated that the empirical forms do indeed constitute the true asymptotic state of the polarized magnetic Thomson transfer system.

A further, independent check was to actually fold the analytic forms in Eqs. (24), (27) and (28) through the phase matrix analysis formulation of Chou (1986) numerically. The post-scattering Stokes parameter information was

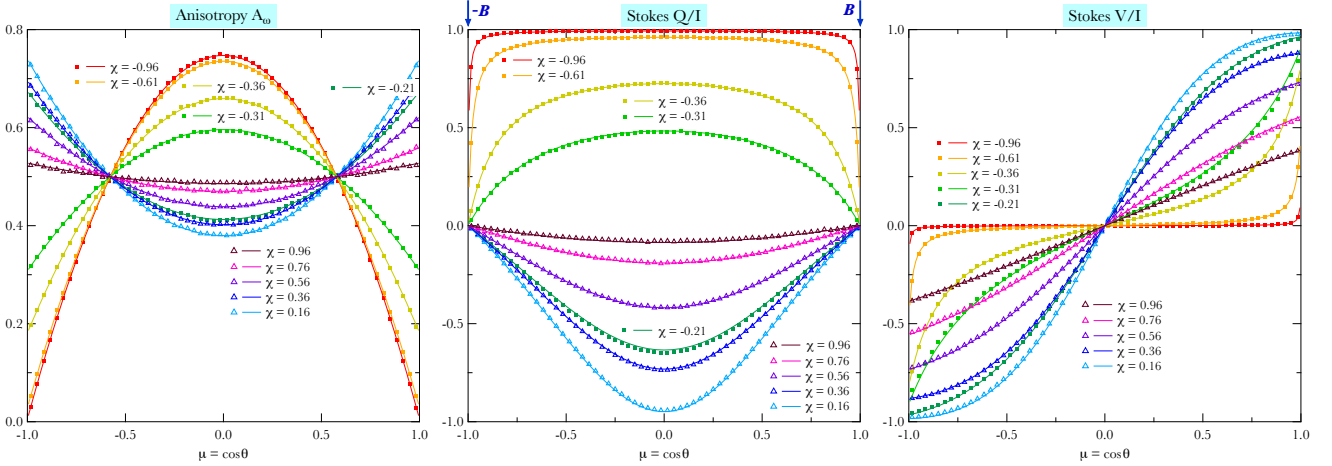


Figure 7. Angular distributions for A_ω (left), Stokes \hat{Q}_ω (center) and Stokes \hat{V}_ω (right) for high opacity runs of radiative transfer at select photon frequencies ω identified by the parameter $\chi = \log_{10}(\omega/\omega_B)$, as labelled. These correspond to horizontal cuts of the respective panels in the frequency-angle maps in Fig. 6. Again, the angle θ is measured relative to \mathbf{B} , as indicated in the middle panel. The squares (for $\chi < 0$) and open triangles (for $\chi > 0$) represent data acquired for the runs with 100 scatterings for each of the $\mathcal{N}/160 = 6.25 \times 10^6$ photons per frequency bin. The curves are computed using the relatively compact analytic forms of the empirical approximations in Eqs. (24), (27) and (28), demonstrating the precision of these fits at around the 2% level or better.

obtained via numerical integration over the phase matrix form in Eq (2.24) of Barchas (2017), adapted from Whitney (1991a), over scattering solid angles and weighted by the pre-scattering Stokes parameters. The two frequency-dependent functions $\mathcal{A}(\omega)$ and $\mathcal{C}(\omega)$ were left as free parameters, and their values for each ω were derived numerically by demanding that the Stokes parameters were invariant under the scattering operation. The solution for these two functions agreed numerically with the empirical determinations in Eqs. (26) and (29) to excellent precision. Details of this validation protocol will be expanded in a future paper.

Note that in hydrostatic models of magnetar atmospheres, radiation at $\omega/\omega_B \ll 1$ is dominated by \perp mode photons ($Q < 0$) because they emerge from hotter regions deep in the atmosphere (e.g. Özel 2001; Ho et al. 2003) where they are more numerous. This property is not evident in the Q/I panels of Figs. 6 and 7 since temperature weighting and stratification are currently not included in our simulation.

5.3 Interpreting the Re-distribution Anisotropy

To correctly interpret the simulation results presented in Section 5.1, it is necessary to identify the relationship between the intensity $I(\mu)$ and the re-distribution anisotropy $A_\omega(\mu)$, and extend such to all Stokes parameters. What is output from the high opacity simulation are the statistics of all the pertinent products of electric field components, averaged per scattering. These data are not generated in the spatial or radiative transfer domain. As such, they represent conditional probabilities of a re-distribution mapping from one polarization/anisotropy configuration to another, i.e., defining the probability of a scattering into new directions and new polarization vectors given these quantities prior to the photon scattering. The mapping function is a 4-tensor or matrix \mathcal{R} in polarization space, and will be termed the **re-distribution tensor** or **phase matrix** (Chou 1986) for magnetic Thomson scattering. For an unpolarized scattering process, i.e. one-dimensional in polarization space (intensity

only; $Q = U = V = 0$), this must reduce to the differential cross section divided by the total cross section.

Let $\mathbf{S} = (I, Q, U, V)$ be the true Stokes vector and $\mathbf{P} = (I_P, Q_P, U_P, V_P)$ be its corresponding quantity (putatively dimensionless) in the re-distribution mapping. We expect that $\mathbf{S} \propto \mathbf{P}$, with a single coefficient of proportionality that can be dependent on a photon’s direction. The evolution of \mathbf{P} with scattering is negligible in the high scattering limit, and this can be expressed via a “polarization equilibrium” re-distribution equation

$$\mathbf{P}(\mathbf{k}) = \int \mathcal{R}(\mathbf{k}_i \rightarrow \mathbf{k}) \mathbf{P}(\mathbf{k}_i) d\Omega_i \quad . \quad (30)$$

The subscript i denotes initial quantities prior to a scattering, which deflects a photon from direction $\hat{\mathbf{k}}_i$ to $\hat{\mathbf{k}}$. The right hand side of Eq. (30) describes the establishment of a new photon direction and a new photon polarization given a pre-scattering polarization configuration, integrating over all photon directions using the solid angle differential $d\Omega_i$. Setting this equal to the left hand side expresses the asymptotic condition that the system polarization does not change on average in a single scattering, but allows the photon direction to be altered. This precisely describes what is modeled by the high opacity simulations of Section 5.1.

If one were to specialize this re-distribution formalism to unpolarized systems, such as effectively arises in the high opacity “non-magnetic domain” $\omega/\omega_B \gg 1$, then only the I_P portion of \mathbf{P} need be retained. The re-distribution is then in angle only, expressed using the differential cross section, with the structure of a conditional probability leading to a normalizing factor incorporating the total unpolarized cross section. Thus, the analog of Eq. (30) would then be

$$I_P(\mathbf{k}) = \int \frac{1}{\sigma(\mathbf{k}_i)} \frac{d\sigma(\mathbf{k}_i \rightarrow \mathbf{k})}{d\Omega_i} I_P(\mathbf{k}_i) d\Omega_i \quad . \quad (31)$$

Integrating over \mathbf{k} directions ($d\Omega$) one quickly sees that this is properly normalized when introducing the cross section $\sigma(\mathbf{k}_i)$ in the denominator of the integrand. This analogy enables one to directly connect \mathcal{R} with the magnetic Thomson

scattering phase matrix in Eq. (21) of Chou (1986), which expresses the conditional probability weighting via ratios of the differential and total cross section, yet both being dependent on the details of the polarization. Thus, now, $\sigma(\mathbf{k}_i)$ depends on the Stokes parameters, expressed in Eq. (4) of Whitney (1991a), and in Eq. (13) here.

Since Eq. (30) can be scaled by any constant, we can normalize it as suits. Furthermore, our coordinate choices have $U = 0$, so noting $I_P \propto A_\omega(\mu)$, one can write

$$\mathbf{P} = (I_P, Q_P, 0, V_P) \equiv I_P(1, \hat{Q}, 0, \hat{V}) \quad (32)$$

for the interpretation of the simulations in Section 5.1. As the phase matrix version of \mathcal{R} in Eq. (21) of Chou (1986) possesses simple quadratic dependence on both μ_i and μ (final photon angle cosine relative to $\hat{\mathbf{B}}$), the observed quadratic dependence of \mathbf{P} on μ is guaranteed by Eq. (30), and motivates our protocol for seeking its solutions via our Monte Carlo experiment. The numerical evaluations for \mathbf{P} obtained in our simulations nicely satisfy a numerical evaluation of Eq. (30) using the phase matrix of Chou (1986), establishing the correspondence between the two approaches.

The true Stokes vector \mathbf{S} describes fluxes of quadratic forms of electric field components and thus obeys a radiation transport equation. The radiative transfer in polarized scattering systems is expressible as an integro-differential equation (e.g. Chandrasekhar 1960), with the scattering transfer captured in integrals over the differential cross section. This is simplest to express in the unpolarized case, for which only the intensity I comes into consideration. The familiar form for an equilibrium situation with an angular distribution that does not evolve with scatterings can quickly be written down. It is

$$\sigma(\mathbf{k}) I(\mathbf{k}) = \int \frac{d\sigma(\mathbf{k}_i \rightarrow \mathbf{k})}{d\Omega_i} I(\mathbf{k}_i) d\Omega_i \quad , \quad (33)$$

a radiation transfer counterpart to Eq. (31). Thus, one infers that $I_P(\mathbf{k}) \propto \sigma(\mathbf{k}) I(\mathbf{k})$. A partner equation for the photon number density angular distribution $n_\gamma(\mu)$ that satisfies the equilibrium Boltzmann equation (time domain) assumes the same form, noting that $I(\mu) \propto n_\gamma(\mu)$. Extending this to the full polarization configuration, we assert the correspondence

$$\mathbf{P}(\mathbf{k}) \propto \sigma(\mathbf{k}) \mathbf{S}(\mathbf{k}) \quad . \quad (34)$$

This can be inserted into Eq. (30) to develop the radiative transfer analog of Eq. (33) for the full polarization configuration. The desired relationship between the two polarization vectors indicates that the coupling depends on both the direction *and* the polarization of the photons.

Taking the intensity portion of Eq. (34) yields the result

$$n_\gamma(\mu) \propto I(\mathbf{k}) \propto \frac{A_\omega(\mu)}{\sigma(\mathbf{k})} \quad (35)$$

for our azimuthally-symmetric system, where $\sigma(\mathbf{k}) \rightarrow \sigma(\omega, \mu)$. This is the sought-after interpretation of the re-distribution anisotropy $A_\omega(\mu) \propto I_P$, defining a path for using it to obtain true intensity-related anisotropies. The cross section $\sigma(\mathbf{k})$ must be computed using the asymptotic Stokes parameters, inserted into Eq. (13). The resulting $I(\mu)$ or $n_\gamma(\mu)$ can be employed in formal opacity calculations treating magnetic Thomson diffusion. It is notable that while the scaling $1/\sigma(\mathbf{k})$ impacts the intensity component and those for the other Stokes parameters, by forming ratios Q/I and

V/I , this scale factor cancels out, so that \hat{Q} and \hat{V} are invariant under the mapping from re-distribution (\mathbf{P}) space to Stokes (\mathbf{S}) space. This convenience was exploited in the presentations in Sections 5.1 and 5.2.

While the logic leading to the $\mathbf{P} \propto \sigma \mathbf{S}$ correspondence is intuitive and obvious, its verity is also amenable to scrutiny via simulation. To this end, we performed a number of simulations modified from those addressed in Sections 5.1 and 5.2. Instead of the exit criterion of a fixed total number of scatterings, the simulation termination was made when the cumulative distance travelled by each photon exceeded a pre-defined and large value d_{\max} . This was not a constraint on the spatial displacement from the point of injection, but on a linear addition of the pathlengths travelled between each scattering. Thus it incorporated information on the mean free path $\lambda \propto 1/\sigma(\mathbf{k})$ for magnetic Thomson scatterings, and is a true modeling of radiative transfer as opposed to just angle and polarization re-distribution probabilities. This simulation was performed for a representative range of frequencies $0.1 \leq \omega/\omega_B \leq 10$. To excellent precision, the emergent polarization information generated intensity anisotropies $I(\mu) \propto A_\omega(\mu)/\sigma$ and the same $\hat{Q}(\mu)$ and $\hat{V}(\mu)$ distributions produced by the fixed number of scattering simulations of Section 5.1. Results for this comparison will be presented in another paper. These experiments thus numerically validate the $\mathbf{S} \propto \mathbf{P}/\sigma$ relationship.

To complement the $A_\omega(\mu)$ information presented in Fig. 7, we plot in Fig. 8 the resultant intensity anisotropy $I(\mu) \propto n_\gamma(\mu)$ described in Eq. (35). The curves are mostly normalized to unit area, and also represent the intensity anisotropy. Thus, hereafter, we posit the form

$$I(\mu) = \frac{A_\omega(\mu)}{\Lambda_\omega \sigma(\omega, \mu)} \quad , \quad \Lambda_\omega = \int_{-1}^1 \frac{A_\omega(\mu) d\mu}{\sigma(\omega, \mu)} \quad . \quad (36)$$

Again, $\sigma(\omega, \mu)$ is the cross section form in Eq. (13) with the full polarization information embodied in $I_P \rightarrow A_\omega(\mu)$, \hat{Q} and \hat{V} from the empirical approximations of Section 5.2 incorporated. This $I(\mu)$ form will be employed in Section 5.4. It is evident that the overall anisotropy is much smaller than that evinced by $A_\omega(\mu)$. Yet anisotropy is still significant, particularly around $\omega/\omega_B \sim 1/\sqrt{3}$ where the interplay between linear and circular polarizations is complex, and also around $\mu \approx \pm 1$ at lower frequencies. The distributions are approximately isotropic at both the cyclotron resonance and in the non-magnetic regime $\omega \gg \omega_B$.

5.4 High Opacity Slab Simulations

The real utility of developing the connection between re-distribution anisotropy $A_\omega(\mu)$ and the true intensity one, and the three empirical approximations for $A_\omega(\mu)$, $\hat{Q}(\mu)$ and $\hat{V}(\mu)$, is that they circumvent the need to compute atmospheric slabs with large thicknesses and high opacities. Regions deep in the atmospheres that sample $\tau_{\parallel, \perp} \gg 10$ are just zones of high opacity that do not intimately connect to the escape through the upper atmospheric boundary. Accordingly, it is expedient to use the empirical approximations to define suitable polarized and anisotropic injections at the base of the slab, capturing the key information of scattering diffusion deeper in the atmosphere. This can be done simply using an accept/reject procedure. This is performed here for the magnetic polar case to take advantage

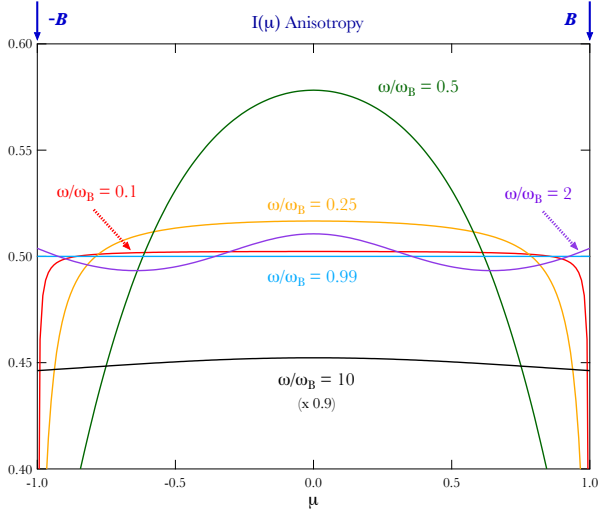


Figure 8. Intensity $I(\mu)$ as a function of $\mu = \cos \theta$, for our six familiar frequencies $\omega/\omega_B = 0.1, 0.25, 0.5, 0.99, 2, 10$. These depictions, germane to high opacity domains, are obtained by dividing the re-distribution anisotropy $A_\omega(\mu)$ in Eq. (24) by the polarized cross section in Eq. (13): see Eq. (36). All polarization information was generated using Eqs. (27) and (28), and the empirical approximations in Eqs. (26) and (29). Distributions were normalized to unity on $[-1, 1]$; the $\omega/\omega_B = 10$ curve was multiplied by 0.9 to aid visual clarity.

of its azimuthal symmetry, though in principle the following injection protocol can be modified routinely through rotations to address any field orientation in the slab.

First, the direction of the injected photon is specified exactly as before via Eq. (17) in using two variates ξ_θ and ξ_ϕ selected randomly on the interval $[0, 1]$. These establish the angles θ_0 and ϕ_0 , respectively, and the azimuthal symmetry guarantees that the value of ϕ_0 can always be accepted. In contrast, as the polar angle injection distribution is not isotropic in general, we introduce a new random variate ξ_I on the interval $[0, I_{\max}]$ for the intensity anisotropy. Here, I_{\max} is the maximum value of $I(\mu_0)$ on the interval $-1 \leq \mu_0 \leq 1$ (see Fig. 8). Then, if $\xi_I \leq n_\gamma(\mu_0)$ for $\mu_0 \equiv \cos \theta_0$, the polar angle is accepted, otherwise new ξ_θ and ξ_I variates are chosen and the process repeated until an acceptance occurs. The injection is then further flux-weighted by a factor of μ_0 as with all prior slab runs.

The polarization injection protocol is similarly expedient, employing the electric field vector forms in Eq. (12). Each photon has a scaled intensity of $\hat{I}_0 = 1$, and the polarization degree Π for the injection is given by the combination of information from Eqs. (27) and (28):

$$\Pi = \sqrt{(\hat{Q}_0)^2 + (\hat{V}_0)^2}, \quad (37)$$

for

$$\hat{Q}_0 = \hat{Q}_\omega(\mu_0), \quad \hat{V}_0 = \hat{V}_\omega(\mu_0). \quad (38)$$

A new random variable ξ_Π is sampled on $[0, 1]$ to determine the polarization state of the photon. If $\xi_\Pi \geq \Pi$, then the injection is deemed unpolarized, and it is sufficient to randomly select linear modes of either the \parallel state ($\hat{\mathcal{E}}_\theta = 1, \hat{\mathcal{E}}_\phi = 0$) or the \perp one ($\hat{\mathcal{E}}_\theta = 0, \hat{\mathcal{E}}_\phi = 1$). With large photon count statistics, this generates unpolarized information, and a $+/-$ circular polarization choice could

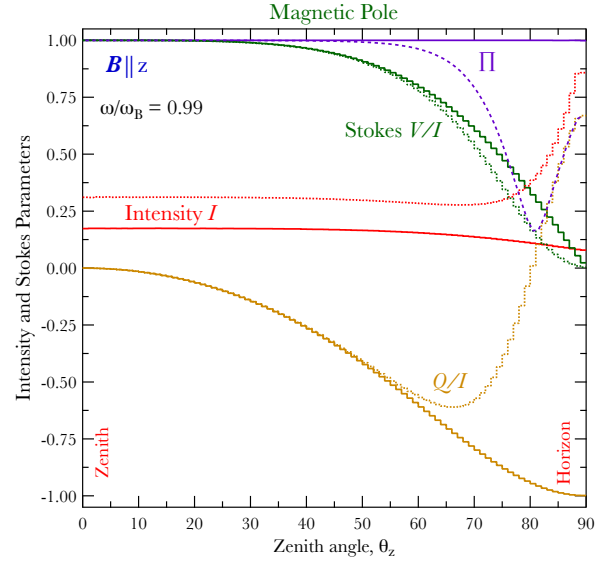


Figure 9. Angular distributions of intensity (red) and Stokes parameters Q/I (tan) and V/I (green) as functions of the zenith angle θ_z , for $\omega/\omega_B = 0.99$ and the polar case where \mathbf{B} is parallel to the slab normal. The purple curves constitute the resultant polarization degree. The solid histograms display the results of $\tau_{\parallel} = 10$ with polarized injection at the slab base using the empirical forms as described in the text for the high opacity simulations. The injection was anisotropic, effectively comprising mixtures of linearly and circularly-polarized photons so that the ensemble satisfies Eqs. (24), (27) and (28). The dotted histograms/curves are from the $\omega/\omega_B = 0.99$ panels of Figs. 2 and 3, displaying the results for isotropic injection for a slab depth of $\tau_{\parallel} = 10$.

also be implemented. If, on the other hand, $\xi_\Pi < \Pi$, the injected photon is polarized, and one can choose \mathcal{E}_θ to be real without loss of generality, which implies that \mathcal{E}_ϕ is purely imaginary. The inversion of Eq. (12) then yields

$$\hat{\mathcal{E}}_\theta = \sqrt{\frac{\Pi + \hat{Q}_0}{2\Pi}}, \quad \hat{\mathcal{E}}_\phi = \frac{i\hat{V}_0}{2\Pi\hat{\mathcal{E}}_\theta} = i \text{sgn}(\hat{V}_0) \sqrt{\frac{\Pi - \hat{Q}_0}{2\Pi}}. \quad (39)$$

These define an elliptically-polarized photon. In the limits where $\hat{Q}_0 \rightarrow \pm\Pi$, the circular polarization \hat{V}_0 is zero, and these then constitute the \perp and \parallel modes identified just above. For large numbers of photons, this protocol establishes a polarization injection statistically commensurate with the high opacity distributions for \hat{Q} and \hat{V} .

Using this polarized, anisotropic injection protocol, simulations were performed for the magnetic polar cases that were the focus of Figs. 2 and 3, to discern how the introduction of anisotropy and polarization to injection influenced the emergent Stokes parameters at the top of the slab. For the most part, the various distributions were fairly similar to the isotropic, unpolarized injection case once the optical depth τ_{\parallel} exceed around 7 or so, with either modest or small differences. This is not surprising given that numerous scatterings obscure the injection information. The exception was for the resonant $\omega/\omega_B = 0.99$ example, and results for this frequency are presented in Fig. 9. Therein, a comparison between $\tau_{\parallel} = 10$ results for the updated polarized injection and the Figs. 2 and 3 one is forged. Differences are small for zenith angles $\theta_z \lesssim 45^\circ$, but become significant or large for viewing perspectives somewhat near the slab hori-

zon, i.e. perpendicular to the field. The intensity excess near the horizon observed for the isotropic injection case is eliminated because the scattering depopulates the distribution orthogonal to \mathbf{B} . At the same time, circular polarization becomes somewhat more influential in the resonant transport, and the linear polarization signatures correspond to a preponderance of \perp photons as Q/I approaches -1 .

This cameo comparison illustrates the importance of developing an understanding of the Stokes parameter distributions in high opacity domains germane to the deeper portions of neutron star atmospheres. Our illustrative protocol can be applied to any field orientation, thereby capturing any location on the neutron star surface.

6 DISCUSSION AND CONCLUSION

The polarizations and anisotropies determined here in the high opacity domain directly impact the effective Eddington limiting X-ray luminosity for a magnetized compact object, above which radiation pressure-driven winds arise. The familiar non-magnetic value, $L_{\text{Edd}} = 4\pi GM_{\text{NS}}c m_p / \sigma_{\text{T}}$ for a stellar mass M_{NS} (e.g., Rybicki & Lightman 1979), is predicated upon isotropic scattering with the Thomson cross section σ_{T} . This is strongly modified by the magnetic field, particularly well below the cyclotron frequency. Paczynski (1992) employed an angle-averaged Rosseland mean opacity in adapting the Eddington limit to magnetar conditions; various problems with employing such a Rosseland mean were discussed in van Putten, et al. (2013). The polarization-dependent anisotropies and cross sections developed here in Sections 5.1-5.3 can be used to render estimates of the effective Eddington luminosity more precise, leveraging the combination of polarization information embedded in the $A_{\omega}(\mu)$ and $\sigma(\omega, \mu)$, and capturing the important interplay between circular and linear polarization in the vicinity of the cyclotron resonance.

Another potential application of this atmospheric transport simulation is to millisecond pulsars (MSPs). These serve as a prime science focus of NASA’s *NICER* X-ray mission on the International Space Station, with the goal of measuring mass-to-radius ratios that can constrain the neutron star equation of state. In particular, *NICER* has been able to infer a “hot spot” emission geometry for the soft X rays from the surface of MSP J0030+0451 (Riley et al. 2019; Miller et al. 2019) that is far from the antipodal one commonly associated with a pure dipolar configuration for isolated neutron stars. The surface temperature of J0030+0451 (spin period $P = 4.87$ ms) is in the range of $T \sim 1.5 - 3 \times 10^6$ K (0.13 – 0.26 keV; Bogdanov & Grindlay 2009) and its surface polar field is 4.5×10^8 Gauss, establishing a characteristic ω/ω_{B} scale of $3kT/\hbar\omega_{\text{B}} \sim 150$. This corresponds to the non-magnetic domain of our study that is fairly well modeled using the $\omega/\omega_{\text{B}} = 10$ examples in the various figures. The local surface anisotropy, an important quantity for determining contributions to the pulse profile that serves as a principal diagnostic for *NICER*, can be informed by our simulation, for example by $\tau_{\parallel} = 10$ runs like those depicted in the upper left panels of Figures 2 and 5. The anisotropy in this $\omega/\omega_{\text{B}} \gg 1$ regime is very close to that of Sunyaev & Titarchuk (1985), and is approximately independent of the magnetic field orientation in the slab.

Our anisotropy results exhibit general character similar to the non-magnetic, hydrostatic atmosphere results of Zavlin, Pavlov & Shibano (1996). Yet there are differences between their anisotropies and those here, dictated by the significant contributions of free-free and bound-free opacities at low field strengths. Figure 1 of the hydrostatic atmosphere model of Ho & Lai (2001) demonstrates that free-free absorption dominates scattering opacity at energies below 1–2 keV and deeper ($\rho \gtrsim 1 \text{ g cm}^{-3}$) in a stratified, dense atmosphere of a magnetar. Future enhancement of the *MAGTHOMSCATT* simulation will include such free-free opacity, simply implemented in the Monte Carlo technique. The radiation transfer equation solution of Ho & Lai (2001), which is developed for magnetic fields along the slab zenith (polar case), is extrapolated to arbitrary field orientations using a simplistic diffusion approximation. While this is likely suitable for MSP studies, our code’s facility in treating arbitrary field orientations will afford a profound improvement for magnetars and accreting X-ray pulsars, for which departures from radiation isotropy are significant and the diffusion approximation is no longer valid.

While the simulation was constructed using magnetic Thomson scattering for cold electrons in atmospheres, it is routinely generalizable to incorporate the Doppler boosting/broadening and aberration effects associated with warm plasma. It thus has good potential for application to the more tenuous environs of magnetar magnetospheres, for example in modeling magnetar burst emission in hard X rays. This is a problem that has been explored by Taverna & Turolla (2017) in the magnetic Thomson domain via solution of the radiative transfer equation. Such an extension of our Monte Carlo approach will require a suitable reframing of QED scattering cross sections for a domain where the classical formalism focused upon here is no longer appropriate.

In conclusion, this paper presents the details of a versatile Monte Carlo simulation that has been developed to model polarized radiative transfer in neutron star surface layers. The code employs an electric field vector formalism that enables a breadth of utility in terms of the relationship between linear, circular and elliptical polarizations. It is therefore adaptable to address dispersive photon transport in plasmas and the magnetized quantum vacuum. The *MAGTHOMSCATT* code was validated for both intensity and Stokes parameter measures in a variety of ways. The determination of analytic approximations at high optical depths for the Stokes parameters and anisotropy relative to the field direction helps define injection conditions deep in the simulation slab geometries, expediting simulations for full atmospheres, and potentially applicable to other high opacity neutron star magnetospheric environments such as accretion columns and magnetar burst regions.

Our frequency-dependent results identify informative polarization signatures that will be exploited by NASA’s upcoming IXPE X-ray polarimetry mission, presently scheduled for launch in 2021. The next steps in our program will be to integrate results over large surface regions and imbue the code with modules for modeling hydrostatic structure, thereby introducing vertical stratification of temperature, pressure and density into the atmospheres. This will enable exploration of the interplay between photon frequencies and polarization-dependent, photospheric optical depths that is central to signatures of magnetar soft X-ray emission.

ACKNOWLEDGMENTS

The authors thank the referee for comments helpful to improving the communicability of the paper. M. G. B. acknowledges the generous support of the National Science Foundation through grants AST-1517550 and AST-1813649. M. G. B. also thanks the Netherlands Organisation for Scientific Research NWO for support for a visit to the Anton Pannekoek Institute at the University of Amsterdam, where part of the research for this paper was performed.

DATA AVAILABILITY

The data underlying this article is housed on Rice University servers, and will be shared on reasonable request to the corresponding author (M. G. B.).

REFERENCES

- Barchas, J. A. 2017, PhD Thesis, Rice University.
- Baring, M. G., Wadiasingh, Z., & Gonthier, P. L. 2011, *ApJ*, 733, 61
- Becker, W., ed., 2009, *Astrophysics and Space Science Library* Vol. 357, *Neutron Stars and Pulsars*. Springer, Berlin, Heidelberg, p. 91
- Beloborodov, A. M., & Li, X. 2016, *ApJ*, 833, 261
- Blandford R. D. & Scharlemann E. T., 1976, *MNRAS*, 174, 59
- Bogdanov S., Grindlay J. E., 2009, *ApJ*, 703, 1557
- Börner, G., & Meszaros, P. 1979, *Plasma Physics*, 21, 357
- Bulik, T., & Miller, M. C. 1997, *MNRAS*, 288, 596
- Burnard D. J., Arons J. & Klein R. I., 1991, *ApJ*, 367, 575
- Canuto, V., Lodenguai, J., & Ruderman, M. 1971, *Phys. Rev. D*, 3, 2303.
- Chandrasekhar, S. 1960, *Radiative Transfer* (New York: Dover)
- Chou C. K., 1986, *Ap&SS*, 121, 333
- Duncan, R. C. & Thompson, C. 1992, *ApJL*, 392, L9
- Fernández, R., & Thompson, C. 2007, *ApJ*, 660, 615
- Fernández, R., & Davis, S. W. 2011, *ApJ*, 730, 131
- Gnedin I. N., & Sunyaev R. A., 1974, *A&A*, 36, 379
- Gonthier, P. L., Baring, M. G., Eiles, M. T., et al. 2014, *Phys. Rev. D*, 90, 043014
- Gotthelf, E. V., & Halpern, J. P. 2005, *ApJ*, 632, 1075
- Gotthelf, E. V., Perna, R., & Halpern, J. P. 2010, *ApJ*, 724, 1316
- Hamada, T., & Kanno, S. 1974, *Pub. Astron. Soc. Japan*, 26, 421.
- Hambaryan, V., Suleimanov, V., Schwope, A. D., et al. 2011, *A&A*, 534, A74
- Harding, A. K., & Daugherty, J. K. 1991, *ApJ*, 374, 687
- Herold, H. 1979, *Phys. Rev. D*, 19, 2868
- Ho, W. C. G., & Lai, D. 2001, *MNRAS*, 327, 1081
- Ho, W. C. G., & Lai, D. 2003, *MNRAS*, 338, 233
- Ho, W. C. G., Lai, D., Potekhin, A. Y., et al. 2003, *ApJ*, 599, 1293
- Ho, W. C. G., Potekhin, A. Y., Chabrier, G. 2008, *ApJSS*, 178, 102
- Jackson, J. D. 1975, *Classical electrodynamics* (Wiley, New York), 2nd ed.,
- Kouveliotou, C., Dieters, S., Strohmayer, T., et al. 1998, *Nature*, 393, 235
- Lai, D., Ho, W. C. G. 2003, *ApJ*, 588, 962
- Landau, L. D. & Lifshitz, E. M. 1975, *The Classical Theory of Fields* (Pergamon Press, Oxford)
- Medin, Z., Lai, D. 2006, *Phys. Rev. A*, 74, 062508
- Medin, Z., Lai, D. 2007, *MNRAS*, 382, 1833
- Mereghetti, S. 2008, *A&ARv*, 15, 225
- Mészáros P., & Bonazzola S., 1981, *ApJ*, 251, 695
- Miller, M. C., Lamb, F. K., Dittmann, A. J., et al. 2019, *ApJL*, 887, L24
- Niemiec, J., & Bulik, T. 2006, *ApJ*, 637, 466
- Nobili, L., Turolla, R., & Zane, S. 2008, *MNRAS*, 386, 1527
- Özel, F. 2001, *ApJ*, 563, 276
- Özel, F. 2003, *ApJ*, 583, 402
- Paczyński B., 1992, *Acta Astron.*, 42, 145
- Pavlov, G. G., Shibano, Yu. A., Ventura, J., et al. 1994, *A&A*, 289, 837
- Potekhin, A. Y. 2014, *Physics Uspekhi*, 57, 735
- Potekhin, A. Y., Lai, D., Chabrier, G., et al. 2004, *ApJ*, 612, 1034
- Riley, T. E., Watts, A. L., Bogdanov, S., et al. 2019, *ApJL*, 887, L21
- Rybicki, G. B., & Lightman, A. P. 1979, *Radiative Processes in Astrophysics* (Wiley-Interscience, New York)
- Shibano, Yu. A., Zavlin, V. E., Pavlov, G. G., et al. 1992, *A&A*, 266, 313
- Stokes, G. G. 1851, *Trans. Cambridge Phil. Soc.*, 9, 399
- Suleimanov V., Potekhin A. Y., Werner K. 2009, *A&A*, 500, 891
- Sunyaev, R. A. & Titarchuk, L. G. 1985, *A&A*, 143, 374
- Taverna, R. & Turolla, R. 2017, *MNRAS*, 469, 3610
- Taverna, R., Turolla, R., Suleimanov, V., et al. 2020, *MNRAS*, 492, 5057
- Thompson, C. & Duncan, R. C. 1995, *MNRAS*, 275, 255
- Thompson, C. & Duncan, R. C. 1996, *ApJ*, 473, 332
- Thompson, C. & Duncan, R. C. 2001, *ApJ*, 561, 980
- Turolla, R., Zane, S., Drake, J. J. 2004, *ApJ*, 603, 265
- van Adelsberg, M., Lai, D. 2006, *MNRAS*, 373, 1495
- van Putten T., Watts A. L., D’Angelo C. R., Baring M. G., Kouveliotou C., 2013, *MNRAS*, 434, 1398
- Ventura J., 1979, *PRD*, 19, 1684
- Viganò, D., Rea, N., Pons, J. A., et al. 2013, *MNRAS*, 434, 123
- Weisskopf, M. C., Ramsey, B., O’Dell, S., et al. 2016, in *Proc. SPIE*, Vol. 9905, *Space Telescopes and Instrumentation 2016: Ultraviolet to Gamma Ray*, 990517
- Whitney, B. A. 1989, Ph.D. Thesis, Univ. Wisconsin, Madison
- Whitney, B. A. 1991, *ApJ Supp.*, 75, 1293
- Whitney, B. A. 1991, *ApJ*, 369, 451
- Yakovlev, D. G., & Pethick, C. J. 2004, *ARA&A*, 42, 169
- Younes, G., Baring, M. G., Kouveliotou, C., et al. 2020, *ApJL*, 889, L27
- Zane, S., Turolla, R., Nobili, L., et al. 2011, *Adv. Space Res.*, 47, 1298
- Zane S., Turolla R., Treves A. 2000, *ApJ*, 537, 387
- Zavlin V. E., Pavlov G. G., Shibano Y. A., 1996, *A&A*, 315, 141
- Zhang, S. N., Feroci, M., Santangelo, A., et al. 2016, in *Proc. SPIE*, Vol. 9905, *Space Telescopes and Instrumentation 2016: Ultraviolet to Gamma Ray*, 99051Q

Appendix A: Developments for the Cross Section

As the vector formalism for magnetic Thomson scattering has only received very limited treatment in the literature before, we outline our developments here at length for future reference. The starting point for the derivations pertaining to the differential and total cross sections is the complex polarization for the scattered photon, specified using Eqs. (6) and (4):

$$\hat{\boldsymbol{\epsilon}}_f = \frac{\hat{\mathbf{k}}_f \times (\hat{\mathbf{k}}_f \times \boldsymbol{\alpha})}{\omega^2 - \omega_B^2} \quad , \quad \boldsymbol{\alpha} = \omega^2 \hat{\boldsymbol{\epsilon}}_i - i\omega\omega_B \hat{\boldsymbol{\epsilon}}_i \times \hat{\mathbf{B}} - \omega_B^2 (\hat{\boldsymbol{\epsilon}}_i \cdot \hat{\mathbf{B}}) \hat{\mathbf{B}} \quad . \quad (40)$$

This can be inserted into the dipole scattering formula to generate the differential cross section in Eq. (7). The squaring of the polarization vector is expedited using standard vector identities:

$$\left[\hat{\mathbf{k}}_f \times (\hat{\mathbf{k}}_f \times \boldsymbol{\alpha}) \right] \cdot \left[\hat{\mathbf{k}}_f \times (\hat{\mathbf{k}}_f \times \boldsymbol{\alpha}^*) \right] = (\hat{\mathbf{k}}_f \times \boldsymbol{\alpha}) \cdot (\hat{\mathbf{k}}_f \times \boldsymbol{\alpha}^*) = \boldsymbol{\alpha} \cdot \boldsymbol{\alpha}^* - (\hat{\mathbf{k}}_f \cdot \boldsymbol{\alpha}) \cdot (\hat{\mathbf{k}}_f \cdot \boldsymbol{\alpha}^*) \quad . \quad (41)$$

This defines the numerator for the differential cross section in Eq. (7). Expressing $\boldsymbol{\alpha}$ in terms of its real and imaginary vector components, $\boldsymbol{\alpha} = \boldsymbol{\alpha}_R + i\boldsymbol{\alpha}_I$, one can establish the following identities expressed in terms of real and positive-definite quantities:

$$\boldsymbol{\alpha} \cdot \boldsymbol{\alpha}^* = |\boldsymbol{\alpha}_R|^2 + |\boldsymbol{\alpha}_I|^2 \quad , \quad \boldsymbol{\alpha} \cdot \boldsymbol{\alpha}^* - (\hat{\mathbf{k}}_f \cdot \boldsymbol{\alpha}) \cdot (\hat{\mathbf{k}}_f \cdot \boldsymbol{\alpha}^*) = |\boldsymbol{\alpha}_R|^2 + |\boldsymbol{\alpha}_I|^2 - (\hat{\mathbf{k}}_f \cdot \boldsymbol{\alpha}_R)^2 - (\hat{\mathbf{k}}_f \cdot \boldsymbol{\alpha}_I)^2 \quad . \quad (42)$$

From the last identity herein, the following inequality then immediately follows:

$$0 \leq (\hat{\mathbf{k}}_f \times \boldsymbol{\alpha}) \cdot (\hat{\mathbf{k}}_f \times \boldsymbol{\alpha}^*) \leq \boldsymbol{\alpha} \cdot \boldsymbol{\alpha}^* \quad , \quad (43)$$

a result that is of considerable use in posing the accept-reject protocol for choosing the direction of the scattered photon and its associated polarization: see Eq. (19). By inspection of the form for $\boldsymbol{\alpha}$ in Eq. (4), it is apparent that there are domains where $|\boldsymbol{\alpha}_R| \gg |\boldsymbol{\alpha}_I|$ if $\boldsymbol{\epsilon}_i$ is real, for which $\boldsymbol{\alpha} \cdot \boldsymbol{\alpha}^* \approx |\boldsymbol{\alpha}_R|^2 - (\hat{\mathbf{k}}_f \cdot \boldsymbol{\alpha}_R)^2$ and the differential cross section is maximized when $\hat{\mathbf{k}}_f$ is approximately orthogonal to $\boldsymbol{\alpha}_R$. This situation is intuitively expected given the $\hat{\boldsymbol{\epsilon}}_f \propto \hat{\mathbf{k}}_f \times (\hat{\mathbf{k}}_f \times \boldsymbol{\alpha})$ form.

The determination of the total cross section requires the integration of the forms in Eq. (42) over all solid angles, $d\Omega_f$. The polar coordinates for such an integration can be aligned relative to any vector $\boldsymbol{\beta}$. From this one deduces that

$$\int |\boldsymbol{\beta}|^2 d\Omega_f = 4\pi |\boldsymbol{\beta}|^2 \quad \text{and} \quad \int (\hat{\mathbf{k}}_f \cdot \boldsymbol{\beta})^2 d\Omega_f = \frac{4\pi}{3} |\boldsymbol{\beta}|^2 \quad , \quad \text{for } \boldsymbol{\beta} = \boldsymbol{\alpha}_R, \boldsymbol{\alpha}_I \quad . \quad (44)$$

It follows that

$$\int \left[(\hat{\mathbf{k}}_f \times \boldsymbol{\alpha}) \cdot (\hat{\mathbf{k}}_f \times \boldsymbol{\alpha}^*) \right] d\Omega_f = \frac{8\pi}{3} \left\{ |\boldsymbol{\alpha}_R|^2 + |\boldsymbol{\alpha}_I|^2 \right\} = \frac{8\pi}{3} \boldsymbol{\alpha} \cdot \boldsymbol{\alpha}^* \quad . \quad (45)$$

This identity establishes the form for the total cross section in Eq. (8). An alternative path to its derivation is directly via the last identity in Eq. (41), using direct solid angle integration. This employs the result

$$\int (\hat{\mathbf{k}}_f \cdot \boldsymbol{\beta}) (\hat{\mathbf{k}}_f \cdot \boldsymbol{\gamma}) d\Omega_f = \boldsymbol{\gamma} \cdot \boldsymbol{\beta} \int (\hat{\mathbf{k}}_f \cdot \hat{\boldsymbol{\beta}})^2 d\Omega_f + \int (\hat{\mathbf{k}}_f \cdot \boldsymbol{\beta}) \left(\hat{\mathbf{k}}_f \cdot [\boldsymbol{\gamma} - (\boldsymbol{\gamma} \cdot \hat{\boldsymbol{\beta}}) \hat{\boldsymbol{\beta}}] \right) d\Omega_f = \frac{4\pi}{3} \boldsymbol{\gamma} \cdot \boldsymbol{\beta} \quad . \quad (46)$$

The manipulation here is to resolve the vector $\boldsymbol{\gamma}$ into components parallel to $[(\boldsymbol{\gamma} \cdot \hat{\boldsymbol{\beta}}) \hat{\boldsymbol{\beta}}]$ and perpendicular to $\boldsymbol{\beta}$, yielding respectively the first and second integrals in the middle expression. The second integral is simply demonstrated to be zero.

It is straightforward to express the differential cross section in terms of the incoming polarization vector $\hat{\boldsymbol{\epsilon}}$ and $\hat{\mathbf{B}}$ using Eq. (4). When squaring, the last form in Eq. (41) is preferred, and the first portion of this is routinely generated:

$$\boldsymbol{\alpha} \cdot \boldsymbol{\alpha}^* = \omega^4 + \omega_B^2 (\omega_B^2 - 2\omega^2) \left| \hat{\boldsymbol{\epsilon}}_i \cdot \hat{\mathbf{B}} \right|^2 + \omega^2 \omega_B^2 \left| \hat{\boldsymbol{\epsilon}}_i \times \hat{\mathbf{B}} \right|^2 + 2i\omega^3 \omega_B \hat{\mathbf{B}} \cdot (\hat{\boldsymbol{\epsilon}}_i \times \hat{\boldsymbol{\epsilon}}_i^*) \quad . \quad (47)$$

The only notes for deriving this identity are that the $i\omega\omega_B^3$ term is identically zero because of orthogonality of $\hat{\boldsymbol{\epsilon}} \times \hat{\mathbf{B}}$ and $\hat{\mathbf{B}}$, and the cyclic permutation of the triple scalar product is employed to distill the $i\omega^3\omega_B$ term into a convenient form. With this identity, the expanded form for the total cross section in Eq. (9) follows. The remaining term on the right of Eq. (41) is routinely evaluated to generate the full differential cross section:

$$\begin{aligned} \frac{(\omega^2 - \omega_B^2)^2}{r_0^2} \frac{d\sigma}{d\Omega_f} &= \omega^4 \left\{ 1 - (\hat{\mathbf{k}}_f \cdot \hat{\boldsymbol{\epsilon}}_i)^2 \right\} + \omega_B^4 \left| \hat{\boldsymbol{\epsilon}}_i \cdot \hat{\mathbf{B}} \right|^2 \left\{ 1 - (\hat{\mathbf{k}}_f \cdot \hat{\mathbf{B}})^2 \right\} + \omega^2 \omega_B^2 \left\{ \left| \hat{\boldsymbol{\epsilon}}_i \times \hat{\mathbf{B}} \right|^2 - 2 \left| \hat{\boldsymbol{\epsilon}}_i \cdot \hat{\mathbf{B}} \right|^2 \right\} \\ &+ \omega^2 \omega_B^2 \left\{ - \left| \hat{\mathbf{k}}_f \cdot (\hat{\boldsymbol{\epsilon}}_i \times \hat{\mathbf{B}}) \right|^2 + (\hat{\mathbf{k}}_f \cdot \hat{\mathbf{B}}) \left[(\hat{\mathbf{k}}_f \cdot \hat{\boldsymbol{\epsilon}}_i) (\hat{\boldsymbol{\epsilon}}_i^* \cdot \hat{\mathbf{B}}) + (\hat{\mathbf{k}}_f \cdot \hat{\boldsymbol{\epsilon}}_i^*) (\hat{\boldsymbol{\epsilon}}_i \cdot \hat{\mathbf{B}}) \right] \right\} \\ &+ i\omega^3 \omega_B (\hat{\boldsymbol{\epsilon}}_i \times \hat{\boldsymbol{\epsilon}}_i^*) \cdot \left[\hat{\mathbf{k}}_f \times (\hat{\mathbf{k}}_f \times \hat{\mathbf{B}}) \right] + i\omega\omega_B^3 (\hat{\mathbf{k}}_f \cdot \hat{\mathbf{B}}) (\hat{\boldsymbol{\epsilon}}_i \times \hat{\boldsymbol{\epsilon}}_i^*) \cdot \left[\hat{\mathbf{B}} \times (\hat{\mathbf{B}} \times \hat{\mathbf{k}}_f) \right] \quad . \end{aligned} \quad (48)$$

This expression will be employed in the algorithm for radiative transfer in the atmosphere, as discussed in Section 3. Using the integral identities in Eqs. (44) and (46) it can be routinely integrated over solid angles to yield the total cross section in Eq. (9), observing that the $i\omega\omega_B^3$ term integrates to zero. It is technically applicable for non-dispersive light propagation where $\omega = |\mathbf{k}_i| = |\mathbf{k}_f|$ and the eigenmodes are purely transverse; this circumstance is modified when dispersion in a magnetized plasma is treated (Canuto et al. 1971). When $\omega \gg \omega_B$ the influence of the magnetic field is negligible, and only the leading term on the RHS of Eq. (48) is retained, yielding the familiar non-magnetic scattering result $d\sigma/d\Omega_f = r_0^2 \{1 - (\hat{\mathbf{k}}_f \cdot \hat{\boldsymbol{\epsilon}}_i)^2\}$.

Appendix B: Cross Section – Special Cases

To aid insight into the radiative transfer simulation elements, some results pertaining to familiar polarization states are presented. Without loss of generality, the magnetic field will be chosen to be in the z -direction so that $\hat{\mathbf{B}} = (0, 0, 1)$. The initial (i) and final (f) electromagnetic wave unit vectors in a scattering event will be specified by spherical polar coordinates

$$\hat{\mathbf{k}}_j = (\sin \theta_j \cos \phi_j, \sin \theta_j \sin \phi_j, \cos \theta_j) \quad \text{for } j = i, f \quad . \quad (49)$$

Considering first two orthogonal linear polarization states, it is customary to identify these as being parallel (\parallel) to the plane defined by $\hat{\mathbf{k}}_j$ and $\hat{\mathbf{B}}$ (ordinary mode), with the second state (denoted \perp) being perpendicular to this plane (extraordinary mode). Thus, the unit electric field vectors of these two orthogonal polarization modes are given by

$$\hat{\mathcal{E}}_{\perp j} \equiv e^{i\varphi_j} \frac{\hat{\mathbf{k}}_j \times \hat{\mathbf{B}}}{|\hat{\mathbf{k}}_j \times \hat{\mathbf{B}}|} = e^{i\varphi_j} (\sin \phi_j, -\cos \phi_j, 0) \quad , \quad \hat{\mathcal{E}}_{\parallel j} \equiv \hat{\mathbf{k}}_j \times \hat{\mathcal{E}}_{\perp j} = e^{i\varphi_j} (\cos \theta_j \cos \phi_j, \cos \theta_j \sin \phi_j, -\sin \theta_j) \quad , \quad (50)$$

observing that $|\hat{\mathbf{k}}_j \times \hat{\mathcal{E}}_{\perp j}| = 1$ is automatically guaranteed for the orthogonal vector triad constituted by $\hat{\mathbf{k}}_j$, $\hat{\mathcal{E}}_{\perp j}$ and $\hat{\mathcal{E}}_{\parallel j}$. Note also that the complex phase φ_j is explicitly introduced to encompass the possibility of complex electric field vectors \mathcal{E}_j . If these forms are inserted into Eq. (12), one quickly determines that $V = 0$ for both linear polarizations. For the initial wave prior to scattering, one can set $\varphi_i = 0$ without loss of generality. Yet, given the forms in Eqs. (6) and (4), it is apparent that for the scattered wave, in general φ_f is non-zero. The linear polarization states in Eq. (50) simply yield $\hat{\mathcal{E}}_{\perp i} \times \hat{\mathcal{E}}_{\perp i}^* = \mathbf{0} = \hat{\mathcal{E}}_{\parallel i} \times \hat{\mathcal{E}}_{\parallel i}^*$, expediting the algebraic development of the differential and total cross sections. In addition, the normalization results

$$|\hat{\mathcal{E}}_{\perp i} \cdot \hat{\mathbf{B}}| = 0 \quad , \quad |\hat{\mathcal{E}}_{\perp i} \times \hat{\mathbf{B}}| = 1 \quad \text{and} \quad |\hat{\mathcal{E}}_{\parallel i} \cdot \hat{\mathbf{B}}| = \sin \theta_i \quad , \quad |\hat{\mathcal{E}}_{\parallel i} \times \hat{\mathbf{B}}| = \cos \theta_i \quad (51)$$

render the evaluation of Eq. (47) simple, since it only depends on quantities for the incident photon. Thus, the total scattering cross section for \perp and \parallel states and the resultant unpolarized (up) cross section $\sigma_{\text{up}} = (\sigma_{\perp} + \sigma_{\parallel})/2$ can be expressed in units of the Thomson cross section $\sigma_{\text{T}} = 8\pi r_0^2/3$:

$$\sigma_{\perp} = \sigma_{\text{T}} \Sigma_{\text{B}}(\omega) \quad , \quad \sigma_{\parallel} = \sigma_{\text{T}} \sin^2 \theta_i + \sigma_{\text{T}} \Sigma_{\text{B}}(\omega) \cos^2 \theta_i \quad \Rightarrow \quad \sigma_{\text{up}} = \frac{\sigma_{\text{T}}}{2} \left\{ \sin^2 \theta_i + \Sigma_{\text{B}}(\omega) [1 + \cos^2 \theta_i] \right\} \quad , \quad (52)$$

with

$$\Sigma_{\text{B}}(\omega) = \frac{\omega^2(\omega^2 + \omega_{\text{B}}^2)}{(\omega^2 - \omega_{\text{B}}^2)^2} = \frac{1}{2} \left\{ \frac{\omega^2}{(\omega - \omega_{\text{B}})^2} + \frac{\omega^2}{(\omega + \omega_{\text{B}})^2} \right\} \quad . \quad (53)$$

Using the second form for $\Sigma_{\text{B}}(\omega)$, which isolates the helicity contributions to the scattering, it is quickly seen that the polarized forms in Eq. (52) are identical to those in Eq. (16) of Herold (1979), who took the non-relativistic limit of a quantum mechanical treatment. An alternative path to the same result is to instead evaluate α in Eq. (4) directly:

$$\alpha_{\perp} = \omega^2 \hat{\mathcal{E}}_{\perp i} - i\omega\omega_{\text{B}} \hat{\mathcal{E}}_{\perp i} \times \hat{\mathbf{B}} \quad , \quad \alpha_{\parallel} = \omega^2 \hat{\mathcal{E}}_{\parallel i} - i\omega\omega_{\text{B}} \cos \theta_i \hat{\mathcal{E}}_{\perp i} + \omega_{\text{B}}^2 e^{i\varphi_i} \sin \theta_i \hat{\mathbf{B}} \quad , \quad (54)$$

observing that the second term for α_{\parallel} is the $\hat{\mathcal{E}}_{\parallel i} \times \hat{\mathbf{B}}$ contribution. These forms quickly yield

$$\alpha_{\perp} \cdot \alpha_{\perp}^* = \omega^2(\omega^2 + \omega_{\text{B}}^2) \quad , \quad \alpha_{\parallel} \cdot \alpha_{\parallel}^* = (\omega^2 - \omega_{\text{B}}^2)^2 \sin^2 \theta_i + \omega^2(\omega^2 + \omega_{\text{B}}^2) \cos^2 \theta_i \quad , \quad (55)$$

and inserting these into Eq. (8) again yields Eq. (52). A depiction of the linearly-polarized cross section is given in Fig. 10. The Figure is labelled with $B \ll B_{\text{cr}}$, the domain for which its classical derivation is formally valid. Yet, at soft X-ray frequencies it can be applied to supercritical fields such as are encountered in magnetars, since the quantum derivation (e.g. Herold 1979) reduces to the classical one as long as $\hbar\omega \ll m_e c^2$. Fig. 10 illustrates the identity of σ_{\perp} and σ_{\parallel} when $\theta_i = 0$, i.e. for photons propagating exactly along \mathbf{B} , evident in Eq. (52). In this special case of aligned incidence, the scaled acceleration vector α in Eq. (4) is always perpendicular to \mathbf{B} and of fixed magnitude, so the wave excites a circular motion of the target electron.

In order to obtain the differential and total cross sections for specific incident *and* scattered polarization states, it is not possible to directly work from Eq. (48) as the coupling between \mathbf{k}_f and polarization state of this scattered wave needs to be isolated. For $p, q = \perp, \parallel$ denoting the polarization states of incident (p) and scattered (q) waves, we write Eq. (7) as

$$\frac{d\sigma_{p \rightarrow q}}{d\Omega_f} = r_0^2 \frac{\mathcal{E}_{qf} \cdot \mathcal{E}_{qf}^*}{|\mathcal{E}_{pi}|^2} = r_0^2 \frac{[\hat{\mathbf{k}}_f \times (\hat{\mathbf{k}}_f \times \alpha_p)] \cdot \hat{\mathcal{E}}_{qf}^*}{(\omega^2 - \omega_{\text{B}}^2)^2} = r_0^2 \frac{|\alpha_p \cdot \hat{\mathcal{E}}_{qf}^*|^2}{(\omega^2 - \omega_{\text{B}}^2)^2} \quad . \quad (56)$$

Herein, $\mathcal{E}_{qf} = (\mathcal{E}_f \cdot \hat{\mathcal{E}}_{qf}) \hat{\mathcal{E}}_{qf}$ is the projection of the polarization vector \mathcal{E}_f onto the unit vector $\hat{\mathcal{E}}_{qf}$. The polarization vector \mathcal{E}_{qf} can be expressed in terms of $\hat{\mathbf{k}}_f$ and α_p through Eq. (6), and for these linear polarization considerations it assumes one of the forms in Eq. (50). In prescribing the last part of Eq. (56) the vector identity $\hat{\mathbf{k}}_f \times (\hat{\mathbf{k}}_f \times \alpha_p) = (\hat{\mathbf{k}}_f \cdot \alpha_p) \hat{\mathbf{k}}_f - \alpha_p$ was employed, together with the transversality condition $\hat{\mathbf{k}}_f \cdot \hat{\mathcal{E}}_{qf}^* = 0$ appropriate for our zero dispersion presumption. Inserting Eq. (50) and Eq. (54) into the final form in Eq. (56), and defining $\phi_{fi} = \phi_f - \phi_i$ as the change in azimuthal angle in a scattering, one quickly obtains forms for the polarization-dependent differential cross sections:

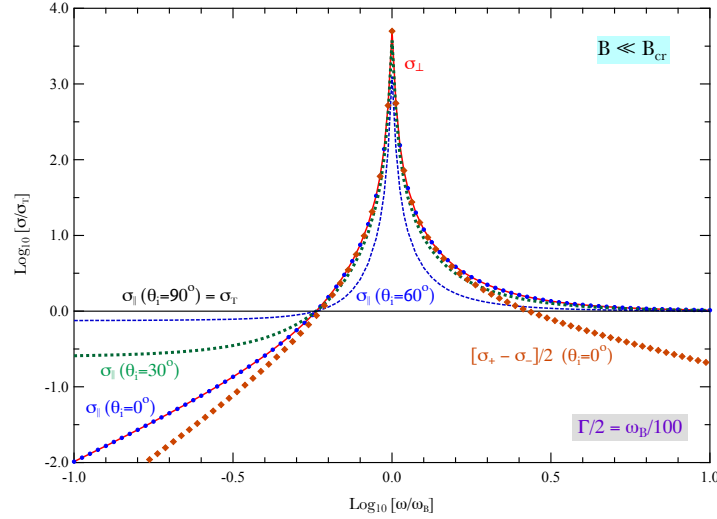


Figure 10. The total cross section $\sigma_{\perp,\parallel}$ for magnetic Thomson scattering (in units of σ_T) for the two standard linear polarization states \perp (extraordinary mode) and \parallel (ordinary mode), computed using Eq. (52) in Appendix B. The cross sections are functions of the frequency ratio ω/ω_B (log scale) and sum over final polarization states. For the \parallel mode, four different incidence angles θ_i to the field direction are depicted, with $\theta_i = 0$ being the blue dots. For the \perp mode (red curve), the cross section is independent of θ_i , and coincides with the $\theta_i = 0^\circ$ result for the \parallel mode. Linear polarization cross sections are resonant at the cyclotron frequency ω_B when $\theta_i < 90^\circ$, truncated using a small width $\Gamma = \omega_B/50$, and are identically equal to the Thomson value σ_T when $\omega = \omega_B/\sqrt{3}$. Also depicted is the difference factor $[\sigma_+ - \sigma_-]/2$ for $\theta_i = 0^\circ$ (brown diamonds) of the cross sections σ_{\pm} for the two circular polarization modes, i.e., the $\Delta_B(\omega)$ circularity function expressed in Eq. (64).

$$\begin{aligned}
 \frac{d\sigma_{\perp \rightarrow \perp}}{d\Omega_f} &= \frac{r_0^2}{(\omega^2 - \omega_B^2)^2} \left(\omega^4 \cos^2 \phi_{fi} + \omega^2 \omega_B^2 \sin^2 \phi_{fi} \right) , \\
 \frac{d\sigma_{\perp \rightarrow \parallel}}{d\Omega_f} &= \frac{r_0^2}{(\omega^2 - \omega_B^2)^2} \cos^2 \theta_f \left(\omega^4 \sin^2 \phi_{fi} + \omega^2 \omega_B^2 \cos^2 \phi_{fi} \right) , \\
 \frac{d\sigma_{\parallel \rightarrow \perp}}{d\Omega_f} &= \frac{r_0^2}{(\omega^2 - \omega_B^2)^2} \cos^2 \theta_i \left(\omega^4 \sin^2 \phi_{fi} + \omega^2 \omega_B^2 \cos^2 \phi_{fi} \right) , \\
 \frac{d\sigma_{\parallel \rightarrow \parallel}}{d\Omega_f} &= r_0^2 \sin^2 \theta_i \sin^2 \theta_f + \frac{r_0^2}{(\omega^2 - \omega_B^2)^2} \left[\cos^2 \theta_i \cos^2 \theta_f \left(\omega^4 \cos^2 \phi_{fi} + \omega^2 \omega_B^2 \sin^2 \phi_{fi} \right) \right. \\
 &\quad \left. + 2\omega^2 (\omega^2 - \omega_B^2) \sin \theta_i \cos \theta_i \sin \theta_f \cos \theta_f \cos \phi_{fi} \right] .
 \end{aligned} \tag{57}$$

All results in Eq. (57) are identical to those in Eq. (1) of Blandford & Scharlemann (1976), which were derived from the classical formalism in Canuto et al. (1971). Integrating these results over the phase difference ϕ_{fi} , and forming the difference between the $\perp \rightarrow \parallel$ and $\parallel \rightarrow \perp$ results, which captures a key portion of the mode switching information, yields

$$\frac{d\sigma_{\perp \rightarrow \parallel}}{d \cos \theta_f} - \frac{d\sigma_{\parallel \rightarrow \perp}}{d \cos \theta_f} = \frac{3}{8} \sigma_T \Sigma_B(\omega) \left\{ \cos^2 \theta_f - \cos^2 \theta_i \right\} . \tag{58}$$

This essentially defines the detailed balance between \perp and \parallel polarizations in the radiative transfer problem, with production of \perp being favored in directions more oblique and perpendicular to the field \mathbf{B} . Integrating Eq. (57) over solid angle yields the total cross section for the four possible linear polarization configurations in units of the Thomson cross section σ_T :

$$\begin{aligned}
 \sigma_{\perp \rightarrow \perp} &= \frac{3}{4} \sigma_T \Sigma_B(\omega) , & \sigma_{\perp \rightarrow \parallel} &= \frac{1}{4} \sigma_T \Sigma_B(\omega) , \\
 \sigma_{\parallel \rightarrow \perp} &= \frac{3}{4} \sigma_T \Sigma_B(\omega) \cos^2 \theta_i , & \sigma_{\parallel \rightarrow \parallel} &= \sigma_T \sin^2 \theta_i + \frac{1}{4} \sigma_T \Sigma_B(\omega) \cos^2 \theta_i .
 \end{aligned} \tag{59}$$

These trivially sum over the final polarizations to produce Eq. (52).

The total cross sections for circular polarized initial states can be derived in a similar way. The unit electric field vectors for the incident photons of positive (subscript +) and negative (subscript -) helicity are given by

$$\hat{\mathcal{E}}_{\pm i} \equiv \frac{1}{\sqrt{2}} (\hat{\mathcal{E}}_{\perp i} \pm i \hat{\mathcal{E}}_{\parallel i}) = \frac{1}{\sqrt{2}} e^{i\varphi_i} \left(\sin \phi_i \pm i \cos \theta_i \cos \phi_i, -\cos \phi_i \pm i \cos \theta_i \sin \phi_i, \mp i \sin \theta_i \right) . \tag{60}$$

If these definitions are inserted into the forms for the Stokes parameters in Eq. (12), one quickly determines that $V_{\pm} = \pm \cos \theta_i$, i.e. when $\theta_i = 0$ and propagation is parallel to $\hat{\mathbf{B}}$, $V = 1$ for the + polarization and $V = -1$ for the - polarization. From

these complex field vectors, one can routinely form $\alpha_{\pm} = (\alpha_{\perp} \pm i\alpha_{\parallel})/\sqrt{2}$, and then employ

$$\left| \hat{\mathcal{E}}_{\pm i} \cdot \hat{\mathbf{B}} \right|^2 = \frac{1}{2} \sin^2 \theta_i \quad , \quad \left| \hat{\mathcal{E}}_{\pm i} \times \hat{\mathbf{B}} \right|^2 = \frac{1}{2} (1 + \cos^2 \theta_i) \quad , \quad \hat{\mathbf{B}} \cdot (\hat{\mathcal{E}}_{\pm i} \times \hat{\mathcal{E}}_{\pm i}^*) = \mp i \cos \theta_i \quad . \quad (61)$$

as identities for the circularly-polarized incident radiation, leveraging Eq. (47) to yield

$$\alpha_{\pm} \cdot \alpha_{\pm}^* = \omega^4 + \frac{1}{2} \omega_B^2 (\omega_B^2 - 2\omega^2) \sin^2 \theta_i + \frac{1}{2} \omega^2 \omega_B^2 (1 + \cos^2 \theta_i) \pm 2\omega^3 \omega_B \cos \theta_i \quad . \quad (62)$$

The $\omega^3 \omega_B$ term is not zero because $\hat{\mathcal{E}}_{\pm i}$ and $\hat{\mathcal{E}}_{\pm i}^*$ are not parallel vectors. The total cross sections can then be expressed as

$$\sigma_{\pm} = \frac{1}{2} \sigma_T \sin^2 \theta_i + \frac{\sigma_T}{(\omega^2 - \omega_B^2)^2} \left[\frac{1}{2} \omega^2 (\omega^2 + \omega_B^2) (1 + \cos^2 \theta_i) \pm 2\omega^3 \omega_B \cos \theta_i \right] = \frac{1}{2} (\sigma_{\perp} + \sigma_{\parallel}) \pm \sigma_T \Delta_B(\omega) \cos \theta_i \quad . \quad (63)$$

with the second form isolating a circularity function

$$\Delta_B(\omega) = \frac{2\omega^3 \omega_B}{(\omega^2 - \omega_B^2)^2} = \frac{1}{2} \left\{ \frac{\omega^2}{(\omega - \omega_B)^2} - \frac{\omega^2}{(\omega + \omega_B)^2} \right\} \quad (64)$$

that is depicted in Fig. 10. Eq. (63) is in agreement with Eq. (17) of Herold (1979). The second form highlights the relationship between the circular polarization results and the linear ones. The circularity contribution is an odd function of $\cos \theta_i$, character that maps into an anti-symmetry of Stokes parameter V in the polar angle relative to \mathbf{B} that is ubiquitous in the results presented in Section 5. The circularity is zero when photons propagate perpendicular to the field, $\theta_i = \pi/2$. When $\theta_i = 0$, and the incoming wave eigenstates are those of circular polarization, the circularity is at a maximum and one quickly deduces from Eq. (63) that $\sigma_+ = \sigma_T \omega^2 / (\omega - \omega_B)^2$ is resonant at the cyclotron frequency, but that $\sigma_- = \sigma_T \omega^2 / (\omega + \omega_B)^2$ is not. The positive helicity state drives the scattered electron in the sense it naturally gyrates in the field, precipitating a resonance at the cyclotron frequency. In contrast, the negative helicity state ‘‘opposes’’ the gyration and does not lead to resonant scatterings.

Without detailing lengthy forms for the polarization-dependent differential cross sections, it suffices to posit a circular polarization analog to Eq. (58) that encapsulates the mode switching information:

$$\frac{d\sigma_{-\rightarrow+}}{d\cos\theta_f} - \frac{d\sigma_{+\rightarrow-}}{d\cos\theta_f} = \frac{3}{8} \sigma_T \Delta_B(\omega) (\cos\theta_f - \cos\theta_i) (1 - \cos\theta_f \cos\theta_i) \quad . \quad (65)$$

Thus, when θ_f is small, and less than the typical θ_i involved in a scattering, the production of the $+$ polarization is favored over the generation of the $-$ state, leading to generally positive V , as is observed in the magnetic polar slab simulation results in Fig. 3, and the $0 < \theta < \pi/2$ values for V/I when $\omega > \omega_B/\sqrt{3}$ in the high opacity data displayed in Fig. 6.